Supplemental Data

Systems-level regulation of microRNA networks by miR-130/301 promotes pulmonary hypertension

Thomas Bertero, Yu Lu, Sofia Annis, Andrew Hale, Balkrishen Bhat, Rajan Saggar, Rajeev Saggar, W. Dean Wallace, David J. Ross, Sara O. Vargas, Brian B. Graham, Rahul Kumar, Stephen M. Black, Sohrab Fratz, Jeffrey R. Fineman, James D. West, Kathleen J. Haley, Aaron B. Waxman, B. Nelson Chau, Katherine A. Cottrill, and Stephen Y. Chan

Supplemental Methods

Network Design

To construct the initial PH network, we used a previously described curated set of PH-relevant genes (1). These genes were selected based on their co-occurrence with the search term “pulmonary hypertension” in the Medline (PubMed) database. As we described (1), interactions between network genes were annotated according to a master list of protein-protein interactions (2-6), protein-DNA interactions (7), kinase-substrate interactions (8, 9), and metabolic interactions (10) drawn from several consolidated databases. These interactions together formed a “consolidated interactome,” consisting of 11,643 nodes and 113,765 edges. These edges represented a wide range of functional relationships including transcriptional, translational, and protein level associations. Notably, the consolidated interactome used for these analyses was further expanded to include information detailed in the Reactome Functional Interaction Network (11), which reports coverage of roughly 50% of the human proteome. When mapped onto this expanded consolidated interactome, the curated PH-relevant genes formed a network consisting of 115 nodes and 398 edges, with a largest connected component (LCC) of 105. We refer to the network formed from this set as the “curated PH network.”

In order to capture novel disease genes that may not have been reported in the literature, we also constructed an expanded network which included genes that could be shown to interact extensively with curated PH genes but which were not present in a literature search at the time of network construction. We refer to this larger network as the “expanded PH network” (listed in Table S1). In order to generate the expanded PH network, we first defined a set of “PH interactors.” An interactor was defined as any node in the consolidated interactome that (a) shared at least one edge with at least one gene in the curated PH network, and (b) was not itself a member of the curated PH network. We then ranked these interactors by their shortest-

path betweenness centrality score, considering only shortest paths between curated PH network genes. Broadly speaking, the shortest-path betweennness centrality (12) of a node *v* in a network *G* represents the amount of network connectivity that would be lost were *v* to be removed from *G*.

$$\text{Eq 1: } C_B(v) = \Sigma_{t \neq t} \sigma_{st}(v) / \sigma_{st}$$

Where *v* is a PH interactor, *s* and *t* are curated PH network genes, σ_{st} represents the number of shortest paths from node *s* to node *t* in the consolidated interactome, and $\sigma_{st}(v)$ represents the number of such paths that must pass through node *v*. This process was performed iteratively. For each iteration, the highest scoring node was incorporated into the PH network, and the betweenness centrality scores of the remaining interactors were recomputed to reflect this change. When the normalized betweenness centrality score of the highest scoring interactor fell below a fixed threshold, no further nodes were added to the network. The resulting network contained 249 nodes and 2,274 edges, with the LCC encompassing all 249 nodes.

MiRNA target prediction: MiRNA target prediction was performed using the well-validated algorithm, TargetScan 6.2 (Conserved) algorithm (13). The TargetScan algorithm detects mRNA transcripts with conserved complimentarity to the “seed sequence” (nucleotides 2-7) of a given miRNA. Because of this, miRNAs that share a seed sequence are grouped together as a family and regarded as a single unit by the algorithm. For this reason, we do not distinguish between miRNAs belonging to the same family in any of our statistical analyses.

Network clustering: Clustering was performed using the Reactome FI analysis tool in the Cytoscape 2.8.1 environment (11, 14). This tool uses a spectral partition-based clustering algorithm which partitions networks in order to maximize the density of connectivity within a group (or “cluster”) of genes. This is measured by the modularity (Q) of the graph. Modularity

here is defined as the fraction of edges within a given cluster, minus the fraction that would be expected by chance if the edges in the network were distributed randomly (15). This is computed as follows:

$$\text{Eq 2a: } Q = \Sigma_i^c (e_i - a_i^2)$$

$$\text{Eq 2b: } e_i = \Sigma_j A_{ij}/2m\ \delta(c_i,c_j)$$

$$\text{Eq 2c: } a_i = k_i/2m$$

Where A_{ij} represents the adjacency matrix of graph *G*, k_i represents the degree of node *i* in *G*, *m* represents the total number of edges in *G*, c represents the number of clusters into which *G* is to be partitioned, e_i represents the fraction of edges for which both vertices are contained in cluster *i*, and a_i represents the fraction of edges for which at least one vertex is contained in cluster *i*. In order to cluster the network optimally, the algorithm aims to maximize modularity. When modularity is high, it indicates that the graph has been partitioned in such a way that the number of edges that fall *within* clusters is large, and the number that fall *between* clusters is comparatively small. Thus, this algorithm ensures that clusters are chosen such that the boundaries of each cluster cross as few edges as possible.

Analyses of network architecture

Identification of miRNAs that broadly regulate the expanded PH network **(miRNA spanning score)***:* To identify miRNAs that might serve as broad regulators of multiple nodes and pathways embedded throughout the PH network, we designed an *in silico* network-based strategy to rank miRNAs according to two criteria: (a) the reliability of their predicted interaction with PH-relevant genes and (b) the breadth of their impact on the PH network as a whole. To do so, we defined a metric that we refer to as the "miRNA spanning score." This score is computed as follows:

$$\text{Eq 3: } SPAN(miR) = (CLUST_{miR} / CLUST_{MAX}) + (\log(p_{miR})/\log(p_{MIN}))$$

$CLUST_{miR}$ represents the number of clusters containing at least one target of the miRNA *miR* and p_{miR} represents the hypergeometric p-value for the number of PH-relevant targets in the *miR* target pool. In order to ensure that each component of the score (i.e. number of targeted clusters and hypergeometric p-value) carries roughly equal weight, the components are normalized by their theoretical maximum value. Thus, $CLUST_{MAX}$ represents the total number of clusters in the expanded PH network, and p_{MIN} represents the theoretical minimum p-value, defined as the reciprocal of the number of simulations used to estimate the hypergeometric distribution (100,000 simulations in this case). In this way, all components of the score are computed out of 1, and the overall miRNA spanning score has a maximum possible value of 2. The first term of the score, $CLUST_{miR}$ / $CLUST_{MAX}$, gives a measure of the miRNA's spread within the network. A miRNA whose targets are distributed throughout all clusters in the network is more likely to influence a wider range of disease-relevant processes, compared with a miRNA whose targets are concentrated within a single network cluster. The second term, $\log(p_{miR})/\log(p_{MIN})$, gives a measure of prediction accuracy. Because miRNAs tend to target multiple genes within a given pathway (16), a tendency that is is particularly evident in PH (1), it is reasonable to expect a PH-relevant miRNA to target a large number of PH network genes, relative to the size of its target pool. By relying on the p-value, rather than the absolute number of PH-relevant targets, we avoid rewarding miRNAs for simply having a large number of targets in the TargetScan database. Together, these two measures provide a means of assessing the reliability of the prediction that a given miRNA is involved in disease, as well as a means of estimating the fraction of the network that will be affected, directly or indirectly, when the expression of this miRNA is altered. MiRNAs that perform well, according to this metric, are thus good candidates for exerting a powerful and widespread effect on the PH network.

Identification of downstream pathways controlled by the miR-130/301 family in PH: In order to predict which miR-130/301 family targets and related downstream pathways may be the most

influential in the progression of PH, we performed several different analyses. These strategies were chosen to interrogate, as broadly as possible, the various methods by which a single miRNA could exert global control over a related gene network(s) specific to PH.

(1) Target Spanning Score: To discern which of the miR-130/301 targets likely exerts the broadest influence over the PH network, we developed a spanning score for network nodes, modified from the miRNA spanning score described above (eq. 3). For gene targets, this was computed as follows:

$$\text{Eq 4: } SPAN(v) = (CLUST_v / CLUST_{MAX}) + C_B(v) + (\log(p_{miR})/\log(p_{MIN}))$$

Where C_B represents the shortest-path betweenness centrality score of node *v*, normalized according to the theoretical maximum betweenness centrality score, defined as ½(N-1)(N-2) for an undirected network of N nodes (i.e. the total number of non-redundant node pairs), p_{miR} represents the hypergeometric p-value of the number of targets in *v*'s first degree neighborhood that are also targeted by miR-130/301, and $CLUST_v$, $CLUST_{MAX}$, and p_{MIN} are defined as described above. This score provides a measure both gene *v*'s influence over the network as a whole, as well as miR-130/301's influence over gene *v* and its immediate neighbors. Genes that perform well, according to this metric, can be said to be both highly influential in the disease network as a whole and highly sensitive to the influence of the miR-130/301 family. Thus, they are ideal "bridges" between the activity of the miR-130/301 family and the rest of the expanded PH network.

(2) Gene Spanning Score: To capture non-target genes that may nonetheless participate in the miR-130/301 regulatory pathway, we also ranked all genes in the expanded PH network according to their gene spanning score. For non-targets, this was computed as follows:

$$\text{Eq 5: } SPAN(v) = (CLUST_v / CLUST_{MAX}) + C_B(v) + C_D(v)$$

Where C_D represents the degree of node *v* in the network, normalized according to the theoretical maximum degree, defined as N-1 for a network of N nodes (*i.e*., the total number of nodes not equal to *v*), and $CLUST_v$, $CLUST_{MAX}$, and $C_B(v)$ are all computed as discussed above. Genes that perform well, according to this metric, can be predicted to exert robust control over the PH network. While they need not be targeted directly by the miR-130/301 family, their wide sphere of influence makes them statistically more likely to participate in those functional pathways that participate in the miR-130/301-mediated regulation of disease.

(3) Shared miRNA Influence Score: To capture miRNAs that may be associated with the miR-130/301-dependent regulation of PH, we ranked each conserved miRNA in the TargetScan database according to the hypergeometric p-value of the overlap of its pool of targets and first-degree target interactors with those genes also directly targeted by miR-130/301. MiRNA that perform well according to this metric can be said to have a high degree of functional overlap with the miR-130/301 family.

Plasmids

3'UTR sequence from PPARγ was cloned in the pSI-CHECK-2 vector (Promega) downstream of the Renilla luciferase using XhoI and NotI restrictions sites. Mutagenesis of the putative miR-130-family binding sites was performed using the QuickChange multisite-directed mutagenesis kit (Stratagene/Agilent) according to the manufacturer's protocol. Coding sequence of PPARγ (BC006811) was amplified by polymerase chain reaction (PCR) using high-fidelity polymerase Phusion (Thermo Fisher Scientific) from an MGC cDNA clone (clone ID: 3447380) and inserted in the pCDH-CMV-MCS-EF1-copGFP (System Biosciences) using NheI and NotI restrictions sites. To achieve constitutive expression of HIF-1α, a mutant HIF-1α expression construct that carries alanine substitutions at proline sites targeted by prolyl-hydroxylases (HA-

HIF1alpha P402A/P564ApBabe-puro, a generous gift from W.G. Kaelin (17)) was used. The lentiviral parent vector expressing GFP was used as a control. Stable expression of these constructs in PAECs or PASMCs was achieved by lentiviral transduction. All cloned plasmids were confirmed by DNA sequencing.

Cell Culture and Reagents

Primary human pulmonary arterial endothelial cells (PAECs) were purchased and propagated in EGM-2 cell culture media (Lonza). Experiments were performed at passages 3 to 6. Primary human pulmonary arterial smooth muscle cells (PASMCs) were purchased and propagated in SmGM-2 cell culture media (Lonza). Experiments were performed at passages 3 to 9. HEK293T cells (American Type Culture Collection) were used and cultivated in DMEM containing 10% fetal bovine serum (FBS). Cells were cultured at 37^{o}C in a humidified 5% CO_2 atmosphere. A modular hypoxia chamber at 0.2% oxygen, 94.8% nitrogen and 5% carbon dioxide was used during 24h for hypoxic conditions. Cultured cells were exposed to recombinant human IL-1β at 10 ng.mL^{-}1 (Peprotech). Recombinant human IL-6 (Peprotech) was used at 100 ng.mL^{-}1. Rosiglitazone (Sigma) was used at 10 μM.

Human Plasma Sampling

To collect blood from subjects from the main pulmonary artery, clinically indicated right heart catheterization procedures were performed by standard protocol via a right internal jugular approach under fluoroscopic guidance. The catheter was positioned into the main pulmonary artery, as confirmed by fluoroscopy and hemodynamic waveforms. Blood was then drawn from the distal catheter port and collected in standard vacutainer tubes with K+-EDTA anticoagulant. Plasma was extracted after standard centrifugation of blood, followed by storage at -80^{o}C.

Animals

All animal treatments and analyses were conducted in a controlled and non-blinded manner.

- VHL flox/flox;Cre-ER mice (C57Bl6 background, >10 backcrosses) were a generous gift from W.G. Kaelin (Dana Farber Cancer Institute, Boston). Conditional inactivation of *VHL* was performed by treating 3- week-old *VHL flox/flox;Cre-ER* mice with 2 mg of tamoxifen (Sigma Aldrich) by intraperitoneal injection every other day for 2 doses as we previously described (18), followed by tissue harvest at 10-13 weeks of age. Tissue from tamoxifen-treated, gender- (male), and age-matched VHL flox/flox mice (without the Cre-ER transgene) was used as wildtype comparison (referred to as VHL WT).
- IL-6 transgenic mice (C57Bl6 background) have been described previously (19).
- *BMPR2X* transgenic mice: Briefly, we used the Rosa26-rtTA2 x TetO7-Bmpr2R899X FVB/N mice previously described (20). Control mice expressed the Rosa26-rtTA2 gene only, but were otherwise identically treated. Expression of transgene occurred only after initiation of doxycycline. Adult mice (12-16 weeks of age) were fed doxycycline in normal (low fat) chow for 6 weeks. Echocardiogram and RVSP were performed at 6 weeks as previously described (21) and the animals sacrificed for harvesting of tissues. Lungs were snap frozen in liquid nitrogen immediately upon sacrifice.
- *Schistosoma mansoni*-infected mice: Mice were exposed to *Schistosoma mansoni* ova to cause experimental PH, using a published technique (22, 23). In brief, eight week old C57Bl6/J mice were used for the study. Experimentally exposed mice were intraperitoneally sensitized on day one and then intravenously challenged on day 14 with *S. mansoni* eggs, at a dose of 175 eggs/gram body weight at each timpoint. *S. mansoni* eggs were obtained from homogenized and purified livers of Swiss-Webster mice infected with *S. mansoni* cercariae, provided by the Biomedical Research Institute (Rockville, MD). On day 21, right ventricular catheterization was performed followed by tissue and blood collection. The mice

were anesthetized with ketamine/xylazine and ventilated through a transtracheal catheter. The abdominal and thoracic cavities were opened, and a 1Fr pressure-volume catheter (Millar PVR-1035, Millar Instruments) was placed through the right ventricle apex to transduce the pressure. Blood samples (400 μl) were drawn after catheterization using into a syringe containing 100μl 0.5M EDTA at pH 8.0. Blood samples were centrifuged at 2000g for 20 minutes at 4^{o}C to separate plasma. The remaining blood was flushed out of the lungs with PBS, the right bronchus was sutured, and 1% agarose was instilled into the left lung through the transtracheal catheter. The left lung was removed, formalin-fixed, and processed for paraffin embedding for histology. The right lungs were removed and snap frozen. The right ventricle free wall was dissected off of the heart and weighed relative to the septum and left ventricle to measure hypertrophy (the Fulton index).

- Wildtype mice exposed to chronic hypoxia +/- SU5416: Eight-week-old littermate mice (C57Bl6) were serially injected intraperitoneally with SU5416 (20 mg/kg/weekly dose; Sigma-Aldrich), followed by exposure to normobaric hypoxia (10% O2; OxyCycler chamber, Biospherix Ltd, Redfield, NY) or normoxia (21% O2) for 3 weeks. Right heart catheterization was then performed followed by harvest of lung tissue for RNA extraction or paraffin embedding. Separately, mice were treated in chronic hypoxia as compared with normoxia without SU5416 administration.
- Monocrotaline-treated rats: As previously described (1), male Sprague-Dawley rats (10-14 week old) were injected with 60 mg/kg monocrotaline at time 0; at 0-4 weeks post-exposure, right heart catheterization was performed followed by harvest of lung tissue for RNA extraction or paraffin embedding, as described below (section: Tissue harvest).
- Surgical placement of PA-aortic shunts in juvenile lambs: As previously described (24), pregnant mixed-breed Western ewes (137-141 d gestation, term = 145 d) were anesthetized. Fetal exposure was obtained through the horn of the uterus; a left lateral

thoracotomy was performed on the fetal lamb. With the use of side biting vascular clamps, an 8.0-mm vascular graft was anastomosed between the ascending aorta and main pulmonary artery of the fetal lambs. Four weeks after spontaneous delivery shunt and control (provided by twin pregnancy or age-matched) lambs were anesthetized and catheters were placed to measure hemodynamics including left pulmonary blood flow. After baseline hemodynamics were obtained, peripheral lung was obtained for analysis. At the end of the protocol, all lambs were euthanized with a lethal injection of sodium pentobarbital followed by bilateral thoracotomy as described in the National Institutes of Health Guidelines for the Care and Use of Laboratory Animals.

Isolation of mouse pulmonary vascular endothelial cells

Up to three lobes of lung tissue from a mouse were diced with scissors, to which 100 μL of collagenase D solution (Sigma) was added for a final concentration of 2 mg/ml collagenase D in 4.9 mL HEPES buffer (pH=7.4). After incubation for 30 min at 37°C with automated rotation, 20 μL of DNase I (Sigma, final concentration of 80 U/mL DNase I) was added and incubated on ice for 30 min. The solution was filtered twice by a 70 μm cell strainer (BD Biosciences) to yield a single cell suspension. After two rounds of PBS wash, cell pelleting, and resuspension, the ACK lysing buffer (Gibco) was used to remove erythrocytes. Remained cells were incubated with anti-CD31 MicroBeads (Miltenyi Biotec) and with FITC-conjugated anti-CD31 antibody (Abcam; Ab95692). Single CD31-positive cells were then collected using an autoMACS Pro Separator, per the manufacturer's instructions (Miltenyi Biotec). The purity of CD31-positive cells was confirmed by flow cytometric analysis of FITC-positive cells by a FACScan flow cytometer (BD Biosciences).

In silico determination of transcription factors predicted to bind the promoters of the different members of miR-130/301 family

We consulted ChIPBase (25), a large database of chromatin immunoprecipitation with next generation DNA sequencing (ChIP-Seq) data, to determine which transcription factors might be modulating miR-130/301 family expression under hypoxia. For each member of the miR-130/301 family, we composed a list of all transcription factors thought to target miRNA promoters based on ChIP-Seq experiments performed in human tissues and cell lines. We then cross-referenced these lists to produce a final set of twelve transcription factors thought to target the promoters of at least four out of the five miR-130/301 family members. Finally, we further narrowed this list by consulting the Transcription Factor Encyclopedia for a curated list of known HIF-2α transcriptional targets (26).

Lentivirus production

HEK293T cells were transfected using Lipofectamine 2000 (Life Technologies) with lentiviral plasmids along with packaging plasmids (pPACK, System Biosciences), according to the manufacturer's instructions. Virus was harvested, sterile filtered (0.45 um), and utilized for subsequent infection of PAECs or PASMCs (24-48 hour incubation) for gene transduction.

miRNA target validation by luciferase assay

Adapted from our previously published protocol (18), HEK293T cells were plated in 96-well plates and transfected with 200 ng of pSICHECK-2 constructs and 5 nM of pre-miRNAs using Lipofectamine 2000 (Life Technologies). The medium was replaced 8 hours after transfection with fresh medium containing 10% FCS, L-glutamine. 48 hours after transfection, firefly and *Renilla* Luciferase activities were measured using the Dual-GloTM Luciferase assay (Promega).

BrdU proliferation assay

Exponentially growing cells were transfected, collected at the indicated times and counted. For proliferation assays, 5-bromo-2-uridine (BrdU) was added to the cell culture medium for 1 hour,

and BrdU incorporated into the DNA was revealed using a detection kit (*BrdU* Cell Proliferation Assay Kit #6813, Cell Signaling) according to the manufacturer's instructions.

Caspase 3/7 assay

Caspase 3,7 activity was quantified using the Caspase-Glo 3/7 Assay (Promega), according to manufacturer's instructions. Briefly, cells were plated in triplicate in 96-well plates and transfected with the appropriate oligonucleotide. Forty-eight hours after transfection, cells were cultured in the presence or absence of serum for twenty-four hours. Cells were then incubated for 1h with the caspase substrates, and luminescence was quantified.

Plasma RNA extraction

To remove any residual cellular contents, thawed plasma samples were further centrifuged (13,000 rpm x 10 minutes), and plasma supernatant was aliquoted into 100 ul volumes for storage at -80^{o}C or further analysis. Specifically, to a standard volume of each plasma supernatant (100 μl), 2 picomoles were added of a chemically synthesized miRNA duplex mimic of microRNA-422b (miR-422b) (Life Technologies). Given minimal expression and minimal changes of expression of endogenous miR-422b (27), equivalent levels of exogenously added miR-422b were used for quantitative normalization of miRNA plasma levels, as previously described (27). Plasma miRNA extraction was performed using a microRNA extraction kit (MicroRNA Extraction System, Benevbio).

Messenger RNA and miRNA extraction

Cells and tissues were homogenized in QiaZol reagent (Qiagen) as we previously described (1). Total RNAs including small RNAs were extracted using the miRNeasy kit (Qiagen) according to the manufacturer's instructions. Total RNA concentration was determined using a ND-1000 micro-spectrophotometer (NanoDrop Technologies).

Quantitative RT-PCR of mature miRNAs

Mature miRNA expression was evaluated using TaqMan MicroRNA Assays (Life Technologies/Applied Biosystems) and the Applied Biosystems 7900HT Fast Real Time PCR device (Life Technologies/Applied Biosystems). Expression levels were normalized to RNU48 or snoR55 for human or mouse experiments, respectively, and calculated using the comparative Ct method ($2^{-\Delta\Delta Ct}$) as we previously described (1) .

Quantitative RT-PCR of messenger RNAs

Messenger RNAs were reverse transcribed using the Multiscript RT kit (Life Technologies) to generate cDNA. cDNA was amplified via fluorescently labeled Taqman primer sets using an Applied Biosystems 7900HT Fast Real Time PCR device, as we previously described (1). Fold-change of RNA species was calculated using the formula ($2^{-\Delta\Delta Ct}$), normalized to actin expression.

Immunoblotting and antibodies

Cells were lysed in RIPA buffer (Santa Cruz Biotechnology) and the protein concentration determined using a Bradford assay (Biorad). Protein lysate (40 mg) were resolved by SDS-PAGE and transferred onto a PVDF membrane (Biorad). Membranes were blocked in 5% non-fat milk in TN buffer (50 mM Tris-HCl pH 7.4, 150 mM NaCl) and incubated in the presence of the primary and then secondary antibodies. After washing in TN buffer containing 0.1% Tween, immunoreactive bands were visualized with the ECL system (Amersham Biosciences). Primary polyclonal or monoclonal antibodies to APLN (sc 33469), EDN1 (sc 21625), FGF2 (sc 79), NOS3 (sc 654), PPARγ (sc 7273) and VEGFA (sc 152) were obtained from Santa Cruz Biotechnology. Primary antibodies for STAT3 (#9139) and P-STAT3 (Tyr-705; #9145) were

purchased from Cell Signaling. Primary antibodies against actin (ab 3280), α-smooth-muscle-actin (ab 32575), CD31 (ab28364), and PCNA (ab 29) were obtained from Abcam. Appropriate secondary antibodies (anti-rabbit and anti-mouse) coupled to HRP were used (Santa Cruz Biotechnology).

Tissue harvest

After physiological measurements, blood was extracted by cardiac puncture for future analyses (hematocrit, plasma extraction). By direct right ventricular puncture, the pulmonary vessels were gently flushed with 1 cc of saline to remove the majority of blood cells, prior to harvesting cardiopulmonary tissue. The heart was removed, followed by dissection and weighing of the right ventricle (RV) and of the left ventricle + septum (LV+S). Organs were then harvested for histological preparation or flash frozen in liquid N2 for subsequent homogenization and extraction of RNA and/or protein. To further process lung tissue specifically, prior to excision, lungs were flushed with PBS at constant low pressure (~10mmHg) via right ventricular cannulation, followed by tracheal inflation of the left lung with 10% neutral-buffered formalin (Sigma-Aldrich) at a pressure of ~20cm H_2O. After excision and 16 hours of fixation in 10% neutral-buffered formalin at 25^{o}C, lung tissues were paraffin-embedded via an ethanol-xylene dehydration series, before being sliced into 5µm sections (Hypercenter XP System and Embedding Center, Shandon).

***In situ* hybridization**

The protocol for *in situ* hybridization for miRNA detection was based on a prior report (28). Specifically, 5 µm sagittal lung sections were probed using a 3' fluorescein isothiocyanate (FITC) labeled miRCURY LNA hsa-miR-130a detection probe (Exiqon). The miRCURY LNA scramble-miR probe was used as negative control. Following re-hydration (Sigma) lungs were

formaldehyde-fixed (4% formaldehyde, Sigma) before inactivation of endogenous enzymes by acetylation buffer [873 uL of triethanolamine (Sigma) and 375 uL acetic anhydride (Fisher) in 75 ml distilled water]. Probe annealing (25 nM LNA probe) was performed in hybridization buffer (Sigma, H7782) for 16 hours at RNA-Tm-22^{o}C (62^{o}C). Following serial washes with 2X SSC, 1X SSC and 0.5X SSC (Sigma) at 62^{o}C, immunolabeling was performed with an anti-FITC biotin-conjugated antibody for overnight at 4^{o}C (1:400; Sigma-Aldrich). For detection, development was achieved by adding streptavidin-biotinylated alkaline phosphatase complex (Vector Labs) followed by Nitro blue tetrazolium chloride/5-Bromo–4-chloro–3–indolyl phosphate substrate solution (NBT/BCIP, Roche), and positive staining was evident by a blue color. MiR-130a expression was quantified in the vascular wall of 15-20 resistance pulmonary arteries (<100 μm external diameter in rodents and <200um external diameter in humans) using ImageJ software (NIH).

Immunohistochemistry of human and mouse lung

Lung sections (5 μm) were deparaffinized and high temperature antigen retrieval was performed followed by blocking in TBS/BSA 5%, 10% goat serum and exposure to primary antibody and biotinylated secondary antibody (Vectastain ABC kit, Vector Labs). In most cases, color development was achieved by adding streptavidin-biotinylated alkaline phosphatase complex (Vector Labs) followed by Vector Red alkaline phosphatase substrate solution (Vector Labs). Levamisole was added to block endogenous alkaline phosphatase activity (Vector Labs). Pictures were obtained using an Olympus Bx51 microscope (40x objective). Small pulmonary vessels (<100 μm diameter) present in a given tissue section (>10 vessels per section) that were not associated with bronchial airways were selected for analysis (N>5 animals per group). Intensity of staining was quantified using ImageJ software (NIH). Degree of pulmonary arteriolar muscularization was assessed in paraffin-embedded lung sections stained for α-SMA by

calculation of the proportion of fully and partially muscularized peripheral (<100 μm diameter) pulmonary arterioles to total peripheral pulmonary arterioles, as previously described (29). Medial thickness was also measured in α-SMA stained vessels (<100 μm diameter) using ImageJ software (NIH) and expressed as arbitrary units. All measurements were performed blinded to condition.

Immunohistochemistry to detect shortmer delivery was performed commercially (Wax It Histology Services, *Inc*.). Specifically, formalin fixed paraffin embedded mouse lung sections were deparaffinised in xylene & rehydrated in graded alcohols. Sections were retrieved in Proteinase K, pH8.0, treated with hydrogen peroxide in methanol for blocking endogenous peroxidase activity, and blocked with protein block to reduce background staining. Sections were then incubated with the primary anti-shortmer antibody E5746-B3A (Regulus Therapeutics) at 1:1000 (0.73 μg/ml) or corresponding negative isotype control Rabbit IgG overnight at 4°C. The following day, the sections were incubated with the HRP Labelled Polymer. Positive staining was visualized with DAB chromagen. Sections were counterstained in Mayer's haematoxylin, blued in lithium carbonate, dehydrated in graded alcohols, cleared in xylene, and mounted with permount.

Pulmonary arterial density quantification

For quantitative assessment of pulmonary arterial density, a previously published study protocols were adapted here (30, 31), lungs were paraffin embedded, sectioned, and stained for CD31 in order to identify vascular endothelium. The number of CD31+ pulmonary vessels (<100 μm diameter) was counted in 30 high-power fields (400X) per mouse lung. Fields containing large airways or major pulmonary arteries were avoided to maintain consistency of counts between sections.

Fluorescent microscopy of mouse lung

To process lung tissue specifically for fluorescence microscopy, prior to excision, lungs were flushed with PBS at constant low pressure (~10mmHg) via right ventricular cannulation, followed by tracheal inflation of the left lung in optimal cutting temperature medium (OCT) (Tissue-Tek, Sakura) at a pressure of ~20cm H_2O, followed by cryopreservation in ethanol/dry ice. Tissue was then further embedded in OCT, frozen solid in cryomolds, sectioned on a Microm HM 550 at 10 µm, and stored at −80 °C. Cryosections were then air dried for 10 min at room temperature and rehydrated in 1× PBS for 15 min at room temperature. Sections were washed in 1× PBS, blocked in 1x PBS/BSA3% supplemented with 10% heat-inactivated goat serum for 1 h at room temperature and then probed with appropriate primary antibody overnight at 4 °C. After incubation, slides were washed 3 times with 1× PBS, blocked for 1 h at room temperature and probed with appropriate secondary antibodies in dark room, 1h at room temperature. After washing, slides were mounted in mounting medium containing DAPI (Vectashield, Vector Labs) and sealed with nail polish.

Supplemental References

1. Parikh VN, Jin RC, Rabello S, et al. MicroRNA-21 Integrates Pathogenic Signaling to Control Pulmonary Hypertension: Results of a Network Bioinformatics Approach. *Circulation.* 2012;125:1520-1532.
2. Rual JF, Venkatesan K, Hao T, et al. Towards a proteome-scale map of the human protein-protein interaction network. *Nature.* 2005;437:1173-1178.
3. Stelzl U, Worm U, Lalowski M, et al. A human protein-protein interaction network: a resource for annotating the proteome. *Cell.* 2005;122:957-968.
4. Venkatesan K, Rual JF, Vazquez A, et al. An empirical framework for binary interactome mapping. *Nat Methods.* 2009;6:83-90.
5. Aranda B, Achuthan P, Alam-Faruque Y, et al. The IntAct molecular interaction database in 2010. *Nucleic Acids Res.* 2010;38:D525-531.
6. Ceol A, Chatr Aryamontri A, Licata L, et al. MINT, the molecular interaction database: 2009 update. *Nucleic Acids Res.* 2009;38:D532-539.
7. Wingender E, Chen X, Fricke E, et al. The TRANSFAC system on gene expression regulation. *Nucleic Acids Res.* 2001;29:281-283.
8. Diella F, Gould CM, Chica C, Via A, Gibson TJ. Phospho.ELM: a database of phosphorylation sites--update 2008. *Nucleic Acids Res.* 2008;36:D240-244.
9. Hornbeck PV, Chabra I, Kornhauser JM, Skrzypek E, Zhang B. PhosphoSite: A bioinformatics resource dedicated to physiological protein phosphorylation. *Proteomics.* 2004;4:1551-1561.
10. Lee DS, Park J, Kay KA, Christakis NA, Oltvai ZN, Barabasi AL. The implications of human metabolic network topology for disease comorbidity. *Proc Natl Acad Sci U S A.* 2008;105:9880-9885.

11. Wu G, Feng X, Stein L. A human functional protein interaction network and its application to cancer data analysis. *Genome Biol.* 2010;11:R53.

12. Brandes U. On variants of shortest-path betweenness centrality and their generic computation. *Social Networks.* 2008;30:2.

13. Friedman RC, Farh KK, Burge CB, Bartel DP. Most mammalian mRNAs are conserved targets of microRNAs. *Genome Res.* 2009;19:92-105.

14. Shannon P, Markiel A, Ozier O, et al. Cytoscape: a software environment for integrated models of biomolecular interaction networks. *Genome Res.* 2003;13:2498-2504.

15. Newman ME. Modularity and community structure in networks. *Proc Natl Acad Sci U S A.* 2006;103:8577-8582.

16. Shirdel EA, Xie W, Mak TW, Jurisica I. NAViGaTing the micronome--using multiple microRNA prediction databases to identify signalling pathway-associated microRNAs. *PLoS One.* 2011;6:e17429.

17. Ivan M, Kondo K, Yang H, et al. HIFalpha targeted for VHL-mediated destruction by proline hydroxylation: implications for O2 sensing. *Science.* 2001;292:464-468.

18. Chan SY, Zhang YY, Hemann C, Mahoney CE, Zweier JL, Loscalzo J. MicroRNA-210 controls mitochondrial metabolism during hypoxia by repressing the iron-sulfur cluster assembly proteins ISCU1/2. *Cell Metab.* 2009;10:273-284.

19. Steiner MK, Syrkina OL, Kolliputi N, Mark EJ, Hales CA, Waxman AB. Interleukin-6 overexpression induces pulmonary hypertension. *Circ Res.* 2009;104:236-244, 228p following 244.

20. West J, Niswender KD, Johnson JA, et al. A potential role for insulin resistance in experimental pulmonary hypertension. *Eur Respir J.* 2013;41:861-871.

21. West J, Harral J, Lane K, et al. Mice expressing BMPR2R899X transgene in smooth muscle develop pulmonary vascular lesions. *Am J Physiol Lung Cell Mol Physiol.* 2008;295:L744-755.

22. Graham BB, Chabon J, Kumar R, et al. Protective role of IL-6 in vascular remodeling in Schistosoma pulmonary hypertension. *Am J Respir Cell Mol Biol*. 2013;49:951-959.

23. Graham BB, Chabon J, Gebreab L, et al. Transforming growth factor-beta signaling promotes pulmonary hypertension caused by Schistosoma mansoni. *Circulation.* 2013;128:1354-1364.

24. Reddy V, Meyrick B, Wong J, et al. In utero placement of aortopulmonary shunts. A model of postnatal pulmonary hypertension with increased pulmonary blood flow in lambs. *Circulation.* 1995;92:606-613.

25. Yang JH, Li JH, Jiang S, Zhou H, Qu LH. ChIPBase: a database for decoding the transcriptional regulation of long non-coding RNA and microRNA genes from ChIP-Seq data. *Nucleic Acids Res.* 2013;41:D177-187.

26. Yusuf D, Butland SL, Swanson MI, et al. The transcription factor encyclopedia. *Genome Biol.* 2012;13:R24.

27. Baggish AL, Hale A, Weiner RB, et al. Dynamic Regulation of Circulating MicroRNA during Acute Exhaustive Exercise and Sustained Aerobic Exercise Training *J Physiol.* 2011;589:3983-3994.

28. Pena JT, Sohn-Lee C, Rouhanifard SH, et al. miRNA in situ hybridization in formaldehyde and EDC-fixed tissues. *Nat Methods.* 2009;6:139-141.

29. Hansmann G, Wagner R, Schellong S, et al. Pulmonary arterial hypertension is linked to insulin resistance and reversed by peroxisome proliferator-activated receptor-gamma activation. *Circulation.* 2007;115:1275-1284.

30. Thebaud B, Ladha F, Michelakis ED, et al. Vascular endothelial growth factor gene therapy increases survival, promotes lung angiogenesis, and prevents alveolar damage in hyperoxia-induced lung injury: evidence that angiogenesis participates in alveolarization. *Circulation.* 2005;112:2477-2486.

31. Xia Y, Yang XR, Fu Z, et al. Classical transient receptor potential 1 and 6 contribute to

hypoxic pulmonary hypertension through differential regulation of pulmonary vascular functions. *Hypertension.* 2014;63:173-180.

32. Obad S, dos Santos CO, Petri A, et al. Silencing of microRNA families by seed-targeting tiny LNAs. *Nat Genet.* 2011;43:371-378.

Table S1: Genes in the expanded PH network. Genes are annotated by architectural cluster and PH-relevant functional pathway.

Cluster	Gene	Functional Pathway
Cluster 1	AKT1	TNF Signaling Pathway
	ANGPT4	Angiopoietin Signaling
	BCL2	Apoptosis
	BIRC4	Apoptosis
	KIAA1967	Apoptosis
	CAMK2G	Calcium Signaling Pathway
	KCNA5	Cation Channel Activity
	KCND2	Cation Channel Activity
	KCNIP2	Cation Channel Activity
	TRPC1	Cation Channel Activity
	TRPC3	Cation Channel Activity
	TRPC6	Cation Channel Activity
	SOD2	Mitochondrial Metabolism
	GCH1	Nitric Oxide Synthesis
	GUCY1A2	Nitric Oxide Synthesis
	GUCY1A3	Nitric Oxide Synthesis
	GUCY1B2	Nitric Oxide Synthesis
	GUCY1B3	Nitric Oxide Synthesis
	NOS1	Nitric Oxide Synthesis
	NOS2A	Nitric Oxide Synthesis
	NOS3	Nitric Oxide Synthesis
	PDE1A	Nitric Oxide Synthesis
	PDE1C	Nitric Oxide Synthesis
	PDE2A	Nitric Oxide Synthesis
	PDE3A	Nitric Oxide Synthesis
	PDE6D	Nitric Oxide Synthesis
	PDE7A	Niitric Oxide Signaling
	PDE9A	Nitric Oxide Synthesis
	PTGIR	Prostacyclin
	HSP90AA1	Protein Processing in the ER
	CHUK	TNF Signaling Pathway
	GTF2I	TNF Signaling Pathway
	IKBKE	TNF Signaling Pathway
	MAP1LC3B	TNF Signaling Pathway
	MAPK3	TNF Signaling Pathway
	MAPK8	TNF Signaling Pathway
	NFKB1	TNF Signaling Pathway
	NFKB2	TNF Signaling Pathway
	NFKBIE	TNF Signaling Pathway
	RELA	TNF Signaling Pathway
	TNFSF11	TNF Signaling Pathway
	MAP3K8	TGFbeta Signaling
	IL1B	Vascular Inflammation
	VCAM1	Vascular Inflammation
	ROCK2	Vascular Smooth Muscle Contraction
	ADCY5	Vascular Smooth Muscle Contraction
	AGTR1	Vascular Smooth Muscle Contraction
	CACNA1C	Vascular Smooth Muscle Contraction
	CALM1	Vascular Smooth Muscle Contraction
	FGF2	Vascular Smooth Muscle Contraction
	PRKACA	Vascular Smooth Muscle Contraction
	PRKACB	Vascular Smooth Muscle Contraction
	PRKACG	Vascular Smooth Muscle Contraction
	PRKCA	Vascular Smooth Muscle Contraction
	PRKCB1	Vascular Smooth Muscle Contraction

Continued Table S1		
Cluster	**Gene**	**Functional Pathway**
Cluster 1	PRKCZ	Vascular Smooth Muscle Contraction
	PRKG1	Vascular Smooth Muscle Contraction
	MAPK1	Vascular Smooth Muscle Contraction
	DYNLL1	Other
	DYNLT1	Other
	GFAP	Other
	HIP2	Other
	HMGCR	Other
	MBP	Other
	UBC	Other
Cluster 2	MME	Fibrosis
	MMP1	Fibrosis
	MMP14	Fibrosis
	MMP2	Fibrosis
	MMP3	Fibrosis
	MMP9	Fibrosis
	EPAS1	Hypoxia and Oxygen Homeostasis
	FOS	Hypoxia and Oxygen Homeostasis
	HIF1A	Hypoxia and Oxygen Homeostasis
	HMOX1	Hypoxia and Oxygen Homeostasis
	JUN	Hypoxia and Oxygen Homeostasis
	RBX1	Hypoxia and Oxygen Homeostasis
	SERPINE1	Hypoxia and Oxygen Homeostasis
	SMAD3	Hypoxia and Oxygen Homeostasis
	SP1	Hypoxia and Oxygen Homeostasis
	VHL	Hypoxia and Oxygen Homeostasis
	PDE5A	Nitric Oxide Synthesis
	CDKN2A	P53 Signaling Pathway
	EP300	P53 Signaling Pathway
	PML	P53 Signaling Pathway
	THBS1	P53 Signaling Pathway
	TP53	P53 Signaling Pathway
	APOE	PPAR Signaling Pathway
	ILK	PPAR Signaling Pathway
	LRP1	PPAR Signaling Pathway
	PPARG	PPAR Signaling Pathway
	RXRA	PPAR Signaling Pathway
	PTGIS	Prostacyclin
	PTGS2	Prostacyclin
	AR	Rho Kinase
	CEBPB	Vascular Inflammation
	CYP1B1	Vascular Inflammation
	NFATC2	Vascular Inflammation
	NFATC3	Vascular Inflammation
	VTNR	Vascular Inflammation
	EGR1	Other
	ESR1	Other
	NCOA3	Other
	NOTCH1	Other
	S100A11	Other
	VIP	Other
Cluster 3	APLN	Apelin Signaling
	MDFI	Apelin Signaling
	ANGPT1	Angiopoietin Signaling

Continued Table S1		
Cluster	**Gene**	**Functional Pathway**
Cluster 3	ANGPT2	Angiopoietin Signaling
	BMX	Angiopoietin Signaling
	FN1	Angiopoietin Signaling
	STAT1	Angiopoeitin Signaling
	STAT3	Angiopoietin Signaling
	TEK	Angiopoietin Signaling
	EGF	EGF Pathway
	EGFR	EGF Pathway
	TNC	Fibrosis
	PDGFA	PDGF Pathway
	PDGFB	PDGF Pathway
	PDGFRA	PDGF Pathway
	PDGFRB	PDGF Pathway
	IL13	Vascular Inflammation
	IL1A	Vascular Inflammation
	IL6	Vascular Inflammation
	CAV1	VEGF Signaling
	FYN	VEGF Signaling
	GRB2	VEGF Signaling
	ITGB3	VEGF Signaling
	KDR	VEGF Signaling
	PIK3R1	VEGF Signaling
	PTK2B	VEGF Signaling
	PTPN1	VEGF Signaling
	PTPN11	VEGF Signaling
	SHC1	VEGF Signaling
	SRC	VEGF Signaling
	VEGFA	VEGF Signaling
	PTEN	Other
	SH3KBP1	Other
	SNX2	Other
	GNB2L1	Other
	HLA-DRA	Other
	HLA-DRB5	Other
	HTATIP	Other
	IGF1R	Other
Cluster 4	ACVRL1	TGFbeta Signaling
	BMP2	TGFbeta Signaling
	BMP4	TGFbeta Signaling
	BMP6	TGFbeta Signaling
	BMP7	TGFbeta Signaling
	BMPR1A	TGFbeta Signaling
	BMPR1B	TGFbeta Signaling
	BMPR2	TGFbeta Signaling
	DCN	TGFbeta Signaling
	EIF3I	TGFbeta Signaling
	ENG	TGFbeta Signaling
	FOXG1	TGFbeta Signaling
	GDF5	TGFbeta Signaling
	GREM1	TGFbeta Signaling
	GREM2	TGFbeta Signaling
	PARD3	TGFbeta Signaling
	PPP1CA	TGFbeta Signaling
	SKIL	TGFbeta Signaling
	SMAD1	TGFbeta Signaling
	SMAD2	TGFbeta Signaling

Continued Table S1		
Cluster	**Gene**	**Functional Pathway**
Cluster 4	SMAD4	TGFbeta Signaling
	SMAD5	TGFbeta Signaling
	SMAD6	TGFbeta Signaling
	SMAD7	TGFbeta Signaling
	SMAD9	TGFbeta Signaling
	TGFBI	TGFbeta Signaling
	TGFB1	TGFbeta Signaling
	TGFB2	TGFbeta Signaling
	TGFBR1	TGFbeta Signaling
	TGFBR2	TGFbeta Signaling
	TGFBR3	TGFbeta Signaling
	ZEB1	TGFbeta Signaling
	BTBD2	TGFbeta Signaling
	HIPK2	Other
	PABPC1	Other
	SNRP70	Other
Cluster 5	ADCY1	Endothelin Signaling
	EDN1	Endothelin Signaling
	EDN2	Endothelin Signaling
	EDN3	Endothelin Signaling
	EDNRA	Endothelin Signaling
	PDE6G	Nitric Oxide Synthesis
	HTR1B	Serotonin Signaling
	HTR2B	Serotonin Signaling
	SLC6A4	Serotonin Signaling
	ADRBK1	Thromboxane A2 Receptor Signaling
	GNAI2	Thromboxane A2 Receptor Signaling
	TBXA2R	Thromboxane A2 Receptor Signaling
	TGM2	Thromboxane A2 Receptor Signaling
	CCL2	Vascular Inflammation
	CCL3	Vascular Inflammation
	CCL5	Vascular Inflammation
	CCR1	Vascular Inflammation
	CX3CL1	Vascular Inflammation
	CX3CR1	Vascular Inflammation
	CXCL12	Vascular Inflammation
	HLA-B	Other
	PDCD6IP	Other
Cluster 6	ACTA1	Regulation of Actin Cytoskeleton
	ACTG1	Regulation of Actin Cytoskeleton
	CFL1	Regulation of Actin Cytoskeleton
	CFL2	Regulation of Actin Cytoskeleton
	EZR	Regulation of Actin Cytoskeleton
	LIMK1	Regulation of Actin Cytoskeleton
	LIMK2	Regulation of Actin Cytoskeleton
	ARHGEF12	Rho Kinase
	PAK1	Rho Kinase
	RAC1	Rho Kinase
	RHOA	Rho Kinase
	RHOB	Rho Kinase
	RHOG	Rho Kinase
	ROCK1	Rho Kinase
	ICAM1	Vascular Inflammation
	SELP	Vascular Inflammation
	ADD1	Other

Continued Table S1		
Cluster	**Gene**	**Functional Pathway**
Cluster 7	RTN4	Other
	CSNK1A1	FoxO Family Signaling
	CTNNB1	FoxO Family Signaling
	HSPA5	Protein Processing in the ER
	HSPA8	Protein Processing in the ER
	STUB1	Protein Processing in the ER
	ACTB	Regulation of Actin Cytoskeleton
	REM1	Regulation of Actin Cytoskeleton
	CDKN1B	Vascular Inflammation
	GSK3B	VEGF Signaling
	RPS27A	Other
Cluster 8	DLAT	Mitochondrial Metabolism
	FASN	Mitochondrial Metabolism
	MLYCD	Mitochondrial Metabolism
	PDHA1	Mitochondrial Metabolism
	PDHA2	Mitochondrial Metabolism
	PDHB	Mitochondrial Metabolism
	PDHX	Mitochondrial Metabolism
	PDK1	Mitochondrial Metabolism
	PDK2	Mitochondrial Metabolism
	PDK3	Mitochondrial Metabolism
	PDK4	Mitochondrial Metabolism

Table S2: Top thirty miRNA families ranked by their miRNA spanning score. This spanning score considers (a) the fraction of network clusters targeted by each miRNA and (b) the hypergeometric p-value of the overlap of the target pool of the miRNA with the expanded PH network. P-values were normalized by the theoretical maximum p-value, defined as the reciprocal of the number of simulations used to estimate the distribution (in this case, 100,000 simulations were used).

miRNA	Number of Clusters Targeted	Targets in Network	Targets in TargetScan	p-value	Overall Score
miR-130ac/301ab/301b/301b-3p/454/721/4295/3666	8	28	638	0.00006	1.84437
miR-27abc/27a-3p	8	33	846	0.00007	1.83098
miR-135ab/135a-5p	8	24	515	0.00013	1.777211
miR-204/204b/211	8	23	481	0.00014	1.770774
miR-200bc/429/548a	6	32	771	0.00007	1.58098
miR-155	7	17	329	0.00032	1.57397
miR-33ab/33-5p	6	17	300	0.00013	1.527211
miR-22/22-3p	8	16	362	0.00257	1.518013
miR-15abc/16/16abc/195/322/424/497/1907	8	30	908	0.00467	1.466137
miR-150/5127	6	13	202	0.00028	1.460568
miR-320abcd/4429	7	22	557	0.00176	1.425897
miR-495/1192	6	26	634	0.00047	1.41558
miR-1ab/206/613	6	24	575	0.00054	1.403521
miR-153	6	22	508	0.00064	1.388764
miR-181abcd/4262	6	31	844	0.00069	1.38223
miR-23abc/23b-3p	7	28	809	0.00298	1.380157
miR-221/222/222ab/1928	7	14	307	0.00344	1.367688
miR-182	8	25	792	0.01507	1.364377
miR-149	6	16	325	0.00098	1.351755
miR-128/128ab	8	23	726	0.01991	1.340186
miR-17/17-5p/20ab/20b-5p/93/106ab/427/518a-3p/519d	8	26	853	0.02052	1.337565
miR-218/218a	7	23	649	0.0051	1.333486
miR-96/507/1271	8	23	732	0.02176	1.332468
miR-374ab	6	20	471	0.00126	1.329926
miR-410/344de/344b-1-3p	6	20	480	0.00148	1.315948
miR-139-5p	6	13	254	0.00176	1.300897
miR-29abcd	7	24	721	0.01016	1.273621
miR-132/212/212-3p	6	14	301	0.00265	1.265351
miR-375	6	10	179	0.00323	1.248159
miR-145	6	20	517	0.00396	1.230461

Table S3: PH-relevant targets of the miR-130/301 family ranked according to their target spanning score. This score considers (a) the normalized shortest path betweenness centrality score of the gene, (b) the fraction of network clusters with which the gene interacts, and (c) the hypergeometric p-value for the overlap of the gene's first degree neighborhood with the miR-130/301 target pool. P-values were normalized by the theoretical maximum p-value, defined as the reciprocal of the number of simulations used to estimate the distribution (in this case, 100,000 simulations were used). Betweenness centrality scores were normalized by the theoretical maximum score, defined as 1/2(N-1)(N-2), where N is the number of nodes in the network.

Gene	p-value	Normalized Betweenness Centrality Score	Interacting Clusters	Overall Score
SMAD4	0.0010	0.012537	7	1.637537
ESR1	0.0115	0.020162	7	1.379987
SMAD5	0.0007	0.003846	4	1.292572
MAPK1	0.0351	0.020854	7	1.259528
PPARG	0.0281	0.003426	6	1.141249
TGFBR1	0.0393	0.017649	6	1.119051
SP1	0.1572	0.037286	7	1.113172
AR	0.0507	0.004285	6	1.078033
PRKACB	0.2429	0.010019	7	1.038662
STAT3	0.3270	0.013249	7	1.009612
NCOA3	0.0132	0.003565	4	0.973422
TGFBR2	0.0481	0.015402	5	0.969866
EDN1	0.1735	0.006163	6	0.946338
TGFB2	0.0023	0.002050	2	0.911618
PTEN	0.2854	0.000788	6	0.886925
BMPR1B	0.0889	0.004058	4	0.766833
CXCL12	0.3441	0.001432	5	0.742261
HSPA8	0.6523	0.012750	5	0.684138
ADCY1	0.0869	0.008517	3	0.648762
BMPR2	0.1065	0.009363	3	0.627526
PDE5A	0.1055	0.003419	3	0.622606
PDK1	0.6186	0.004293	4	0.556440
SNX2	0.0634	0.000022	2	0.549500
PDGFRA	0.1024	0.001626	2	0.499051
ZEB1	0.5120	0.000079	3	0.447762
ROCK2	0.2248	0.000918	2	0.412969
ARHGEF12	0.4499	0.000086	2	0.336807
TRPC3	0.4569	0.000583	1	0.210628

Table S4: Top thirty expanded PH network genes ranked according to their gene spanning score. This score which considers (a) the degree of the gene in the expanded PH network, (b) its shortest path betweenness centrality score in the expanded PH network, and (c) the fraction of network clusters with which it interacts. Degrees were normalized by the theoretical maximum degree, defined as N-1, where N is the number of nodes in the network. Betweenness centrality scores were normalized by the theoretical maximum score, defined as 1/2(N-1)(N-2), where N is the number of nodes in the network.

Gene	Degree	Normalized Betweenness Centrality Score	Number of Clusters Targeted	Overall Score
SRC	77	0.065136	7	1.940136
AKT1	63	0.032708	8	1.850889
MAPK3	60	0.027858	8	1.807079
SP1	66	0.037286	7	1.769428
NFKB1	65	0.037156	7	1.756312
EGFR	64	0.037173	7	1.743342
JUN	55	0.023414	8	1.737699
RELA	62	0.024686	7	1.704881
PRKCA	59	0.046845	7	1.688079
MAPK1	60	0.020854	7	1.675075
PIK3R1	50	0.018902	8	1.668252
GRB2	57	0.026861	7	1.642121
PRKACA	52	0.046974	7	1.597298
SMAD2	53	0.023723	7	1.587034
TP53	52	0.023825	7	1.574149
SMAD3	51	0.025814	6	1.568022
ESR1	47	0.020162	7	1.557499
STAT3	45	0.013249	7	1.550586
CAV1	47	0.018252	7	1.503641
SMAD4	45	0.012537	7	1.471952
CALM1	42	0.029327	7	1.449781
MAPK8	43	0.014189	7	1.447630
SMAD1	42	0.016646	7	1.437101
ACTB	38	0.015426	7	1.383932
RHOA	46	0.028132	6	1.375534
CTNNB1	47	0.012331	6	1.372721
EP300	45	0.016247	6	1.350662
FOS	44	0.028030	6	1.349459
UBC	35	0.013388	7	1.342933
YWHAZ	34	0.021789	7	1.338347

Table S5: Top thirty miRNA families ranked according to their shared miRNA influence score. This score considers the hypergeometric p-value of the overlap of their wider target pool (defined as their pool of direct targets and all first degree interactors of those targets), with the direct target pool of the miR-130/301 family. P-values were normalized by the theoretical maximum p-value, defined as the reciprocal of the number of simulations used to estimate the distribution (in this case, 100,000 simulations were used).

miRNA	p-value	Targets and 1st Degree Interactors in PH Network	Overlap with miR-130/301 Target Pool
miR-15abc/16/16abc/195/322/424/497/1907	0.00507	155	24
miR-30abcdef/30abe-5p/384-5p	0.0057	145	23
miR-23abc/23b-3p	0.0068	157	24
miR-197	0.0053	67	14
miR-340-5p	0.00629	168	25
miR-141/200a	0.00631	127	21
miR-196abc	0.00634	68	14
miR-140/140-5p/876-3p/1244	0.00638	83	16
miR-431	0.007	68	14
miR-342-3p	0.0074	69	14
miR-142-3p	0.00823	70	14
miR-346	0.0083	85	16
miR-486-5p/3107	0.0096	71	14
miR-223	0.01057	96	17
miR-146ac/146b-5p	0.01065	50	11
miR-33ab/33-5p	0.01074	122	20
miR-490-3p	0.01109	43	10
miR-758	0.01141	72	14
miR-1ab/206/613	0.01154	162	24
miR-873	0.012	80	15
miR-384/384-3p	0.01234	97	17
miR-876-5p/3167	0.0128	89	16
miR-224	0.01369	81	15
miR-143/1721/4770	0.01374	115	19
miR-376c/741-5p	0.01513	90	16
miR-190/190ab	0.01521	82	15
miR-132/212/212-3p	0.01553	116	19
miR-192/215	0.01622	20	6
miR-326/330/330-5p	0.01688	83	15
miR-148ab-3p/152	0.01733	117	19

Table S6. **Transcription factors predicted to bind the promoters of the different members of miR-130/301 family.** Of twelve regulators with binding sites shared among promoters of all miR-130/301 members, only POU5F1/OCT4 (OCT4, red) was previously found to be a transcriptional target of HIF-2α, thus singling it out as a potential mediator of HIF-2α-dependent up-regulation of the miR-130/301 family.

miR-130a Transcription Factors (From ChIPBase)	**miR-130b Transcription Factors (From ChIPBase)**	**miR-301a Transcription Factors (From ChIPBase)**	**miR-301b Transcription Factors (From ChIPBase)**	**Shared**
BAF155	AP-2alpha	AP-2alpha	AP-2alpha	BAF155
BAF170	AP-2gamma	AP-2gamma	AP-2gamma	CDX2
CDX2	AR	BAF155	AR	CEBPB
CEBPB	BAF155	BAF170	BAF155	ETS1
CTCF	BRG1	BATF	BRG1	HEY1
ETS1	CBP	BDP1	CBP	HNF4A
FOXH1	CDX2	BRF1	CDX2	JUN
FOXP2	CEBPA	BRG1	CEBPA	NFKB
GATA6	CEBPB	CBP	CEBPB	NFYB
GR	CTCF	CDX2	CTCF	**OCT4**
HEY1	E2F4	CEBPB	E2F4	PU.1
HNF4A	E2F6	E2F1	E2F6	TAF1
JUN	EBF	E2F4	EBF	YY1
NANOG	ERalpha	E2F6	ERalpha	
NFYB	ERG	ERalpha	ERG	
NFKB	ETS1	ERG	ETS1	
NRSF	FOS	ETS1	FOS	
OCT-4	FOSL2	FOS	FOSL2	
EP300	FOXP2	GABP	FOXP2	
P63	GATA1	GATA6	GATA1	
PU.1	GATA2	GTF2B	GATA2	
RAD21	HEY1	HA-E2F1	HEY1	
RPC155	HFN4A	HEY1	HNF4A	
RXRA	INI1	HNF4A	INI1	
SMAD2/3	IRF4	INI1	IRF4	
SMAD3	JUN	IRF4	JUN	
SMAD4	JUND	JUN	JUND	
TAF1	MAX	JUND	MAX	
YY1	MED12	MAX	MED12	
	MYC	MED12	MYC	
	NFYA	MYC	NFYA	
	NFYB	NANOG	NFYB	

Continued Table S6				
miR-130a Transcription Factors (From ChIPBase)	**miR-130b Transcription Factors (From ChIPBase)**	**miR-301a Transcription Factors (From ChIPBase)**	**miR-301b Transcription Factors (From ChIPBase)**	**Shared**
	NFKB	NFYA	NFKB	
	NRSF	NFYB	NRSF	
	OCT-4	NFKB	OCT-4	
	PAX5-C20	OCT-4	PAX5-C20	
	POU2F2	PAX5-C20	POU2F2	
	PU.1	PAX5-N19	PU.1	
	RAD21	PBX3	RAD21	
	SETDB1	POU2F2	SETDB1	
	SIN3AK-20	PU.1	SIN3AK-20	
	SIRT6	RPC155	SIRT6	
	SIX5	SIN3AK-20	SIX5	
	SMAD3	SP1	SMAD3	
	SP1	SPDEF	SP1	
	SREBP1	SREBP1	SREBP1	
	STAT1	SREBP2	STAT1	
	STAT2	STAT1	STAT2	
	TAF1	TAF1	TAF1	
	TCF12	TCF12	TCF12	
	TCF7L2	TCF7L2	TCF7L2	
	TR4	USF1	TR4	
	YY1	YY1	YY1	
	ZNF263		ZNF263	

Table S7. Clinical characteristics of PAH patients (for *in situ* miRNA staining)

Patient	Age (yr)	Gender	mPAP (mmHg)	Clinical description
1	34	Female	50	Autopsy, Idiopathic
2	64	Female	55	Autopsy, Idiopathic
3	12	Male	53	Lung transplant, BMPRII mutation
4	16	Male	62	Lung transplant, Idiopathic
5	1	Male	50	Lung resection, Trisomy 21
6	19	Male	48	Lung resection, Idiopathic
Scleroderma-Induced PAH				
Patient	**Age (yr)**	**Gender**	**mPAP (mmHg)**	**Clinical description**
1	68	Female	44	Lung transplant, Scleroderma
2	56	Male	50	Lung transplant, Scleroderma
3	43	Male	37	Lung transplant, Scleroderma
4	51	Male	48	Lung transplant, Scleroderma
5	59	Female	55	Lung transplant, Scleroderma
6	50	Male	33	Lung transplant, Scleroderma
7	67	Male	50	Lung transplant, Scleroderma
8	39	Male	40	Lung transplant, Scleroderma
9	42	Female	57	Lung transplant, Scleroderma
10	46	Male	47	Lung transplant, Scleroderma
11	60	Female	66	Autopsy, Scleroderma
12	54	Female	54	Autopsy, Scleroderma
13	72	Female	53	Autopsy, Scleroderma

Table S8. Clinical characteristics of PH patients (for miRNA quantification in plasma)

Patient	Age (yr)	Gender	mPAP (mmHg)	PVR (dynes.sec.cm^{-5})	PH group (Group 1-5)
1	66	Female	17	146	no PH
2	63	Female	20	81	no PH
3	42	Female	18	136	no PH
4	37	Male	19	122	no PH
5	61	Male	24	115	no PH
6	72	Male	30	131	3
7	68	Male	27	163	3
8	73	Female	39	645	1
9	68	Female	44	333	1
10	73	Female	43	564	1
11	71	Male	40	428	1-3
12	72	Female	39	889	1
13	75	Female	54	924	1
14	35	Male	58	686	1
15	33	Female	48	551	1
16	34	Female	53	686	1
17	67	Female	47	702	1
18	62	Female	53	840	1
19	69	Male	59	756	1

Supplemental Figure Legends

Figure S1: Up-regulation of the miR-130/301 family by inflammatory cytokines IL-1β and IL-6 as well as by siRNA knockdown of *BMPR2* and *CAV1*.

As demonstrated by RT-qPCR, exposure of PAECs or PASMCs with 10ng/mL IL-1β (**A**) or 100ng/mL IL-6 (**B**) for 24 h (black bars) up-regulated miR-301a compared with vehicle-treated (gray bars) cells. Additionally, miR-301b was induced by IL-1β (n=3) in PASMCs (**A**) and in PAECs treated with IL-6 (**B**). Mean expression of miRNAs in vehicle control groups were assigned a fold change of 1, to which relevant samples were compared. (**C)** As demonstrated by RT-qPCR, siRNA knockdown of *BMPR2* or *CAV1* in PAECs (left graph) and PASMCs (right graph) up-regulated miR-130/301 compared with scrambled control (si-NC). However, siRNA knockdown of other factors genetically associated with PAH such as *ACVR1L*, *ENG*, *KCNK3*, and *SMAD9* had negligible effects on miR-130/301 expression. Mean expression of miRNAs in control groups (si-NC) were assigned a fold change of 1, to which relevant samples were compared. (**D)** As demonstrated by RT-qPCR, effective siRNA knockdown was achieved in PAECs (left graph) and PASMCs (right graph) of factors genetically associated with PAH. For each gene transcript, mean expression in control groups (si-NC, light gray) were assigned a fold change of 1, to which relevant samples (transfected with a siRNA specific to that gene, black) were compared. Data are presented as mean ± S.D. (*P<0.05, ** P<0.01).

Figure S2. Up-regulation of the miR-130/301 family by HIF-2α is dependent upon POU5F1/OCT4.

RT-qPCR expression was analyzed for EPAS1/HIF-2α and POU5F1/OCT4 in PAECs **(A-B)** and PASMCs **(C-D)** after transfection with siRNAs specific for OCT4 (si-OCT4), HIF-2α (si-HIF-2α) or siRNA control (si-NC) during 24 h hypoxia (0.2% O_2) compared with normoxia (21% O_2). In

both cell types transfected with si-NC, hypoxia up-regulated EPAS1/HIF-2α and POU5F1/OCT4 compared with normoxia. Knockdown of HIF-2α (si-HIF-2α) inhibited the induction of POU5F1/OCT4 by hypoxia **(B,D)**, thus confirming that HIF-2α up-regulates POU5F1/OCT4. However, knockdown of POU5F1/OCT4 (si-OCT4) did not prevent induction of HIF-2α by hypoxia. **E)** During HIF-2α (si-HIF-2α) or POU5F1/OCT4 (si-OCT4) knockdown in PASMCs, miR-130/301 family members were not induced by hypoxia, in contrast to cells transfected with siRNA control (si-NC). In **(A-D)**, mean levels in control groups exposed to normoxia and siRNA control (21% O2, si-NC) were assigned a fold change of 1, to which relevant samples were compared. In **(E)**, control groups (21% O2, si-NC) were separately assigned a fold change of 1 for each miRNA, to which relevant samples were compared. Data are presented as mean ± SD (*P<0.05 ** P<0.01).

Figure S3: Expression of the miR-130/301 family is up-regulated in lung tissue of various mouse models of PH. A) As demonstrated by RT-qPCR, expression of the miR-130/301 family members in homogenized lung was up-regulated in *VHL* -/- mice (*VHL* -/-; n=8) as compared with control mice (WT; n=10). **B)** Up-regulation of miR-130b and miR-301a/b was observed in IL-6 transgenic mice in normoxia (21% O_2; n=8, light gray) as compared with wildtype littermates (21% O_2; n=8, white). For wildtype littermates, all miR-130/301 family members were up-regulated by hypoxia (10% O_2; n=8, dark gray) as compared with normoxia (21% O_2; n=8, white). Such differences in hypoxic versus normoxic miRNA expression were also observed in IL-6 transgenic mice. Notably, IL-6 transgenic mice exposed to hypoxia (10% O_2; n=8, black) displayed substantially greater expression of all miR-130/301 family members as compared with hypoxic wildtype littermates (10% O_2; n=8, dark gray). **C)** miR-130/301 family members were up-regulated in homogenized lung of transgenic mice expressing a dominant negative BMPR2 (BMPR2X Tg; n=8) as compared with control mice (WT; n=8). In **(A-C)**, mean miRNA levels in

the WT normoxic groups were assigned a fold change of 1, to which all samples were compared. **D)** miR-130/301 family members were up-regulated in homogenized lung of mice suffering from *S. mansoni*-induced PAH (n=4) as compared with non-infected control mice (Control; n=5). Mean miRNA expression in WT control groups was assigned a fold change of 1, to which all samples were compared. For each experiment PH was confirmed by assessment of RVSP. Data are presented as mean ± SEM (*P<0.05, ** P<0.01).

Figure S4: PPARγ is a direct target of miR-130/301 family.

A) Sequence alignment between miR-130a and the 3'UTR of PPARγ highlights a highly conserved putative binding site (gray). **B)** A luciferase reporter assay confirmed the recognition of the binding site in the PPARγ transcript by miR-130a. HEK293T cells were transfected with a luciferase reporter construct carrying a 3' UTR with either the predicted binding site for the miR-130/301 family encoded by the human PPARγ transcript (WT) or scrambled mutant (mut). In combination, cells were transfected with oligonucleotide mimics of miR-130a or control (miR-NC). miR-130a reduced *Renilla* luciferase activity as compared with miR-NC in the setting of the WT binding site, but induced no significant change in the setting of mutant binding site. Luciferase levels in cells transfected with miR-NC were normalized to 1, to which other conditions were compared. Data are presented as mean ± SD (*P<0.05 ** P<0.01).

Figure S5: Comparison of the specificity of miR-130/301 oligonucleotide inhibitors.

A) Overview of the miRNA silencing approach using seed-targeting tiny locked nucleic acid (LNA) molecules. Tiny LNAs were designed as fully LNA-modified oligonucleotides complementary to the seed region of the miR-130/301 family. The high binding affinity of tiny LNA enables functional inhibition of co-expressed members of miRNA seed families, which leads to de-repression of target mRNAs as described previously (32). In the setting of exposure

to hypoxia (0.2% O_2; 24 h) or normoxia (21% O_2; 24h), expression levels of miR-130/301 family members in PAECs (**B**) and PASMCs (**C**) were quantified after transfection with anti-miR-130a versus control (anti-miR-NC) (left panels) or tiny-LNA-130 versus control (tiny-LNA-NC) (right panels). Corresponding with our previous results, in both PASMCs and PAECs, RT-qPCR revealed an up-regulation of the miR-130/301 family in control treated cells in hypoxia (anti-miR-NC 0.2% O_2 or tiny-NC 0.2% O_2) compared to control cells in normoxia (anti-miR-NC 21% O_2 or tiny-NC 21% O_2). In cells treated with anti-miR-130a, miR-130a was specifically down-regulated in both hypoxia and normoxia compared with control cells transfected with anti-miR-NC. Notably, baseline expression and dynamic alterations of other miR-130/301 family members were not affected by anti-miR-130a. In contrast, in cells treated with tiny-LNA-130, all miR-130/301 family members were down-regulated in normoxia and hypoxia compared with cells treated with tiny-LNA-NC. In all panels, mean levels in control groups (Anti-miR-NC 21% O_2 or tiny-LNA-NC 21% O_2) were assigned a fold change of 1, to which relevant samples were compared. Data are presented as mean ± SD (*P<0.05, ** P<0.01).

Figure S6: The miR-130/301 family promotes proliferation in PAECs and PASMCs.

A) Exponentially growing cells were transfected with miR-130a, anti-miR-130a, tiny-LNA-130 or matched controls and counted each day during 3 days. After 3 days, miR-130a increased significantly the number of human PAECs (left panel) and PASMCs (right panel) compared with control (miR-NC). Conversely, inhibition of miR-130a alone (anti-miR-130a) or all the family (tiny-LNA-130) decreased the number of cells compared to the respective control cells (anti-miR-NC and tiny-LNA-NC, respectively. Moreover, in PAECs and PASMCs, inhibition of the miR-130/301 family (tiny-LNA-130) led to a greater decrease in the number of cells compared with anti-miR-130a. **B)** Exponentially growing human PAECs (left panel) and PASMCs (right panel) were transfected with miR-130a or miR-NC and pulsed with BrdU for 1h. In both cell types, miR-130a increased BrdU incorporation and thus proliferation compared with miR-NC. **C)**

Exponentially growing human PAECs (left panel) and PASMCs (right panel) were transfected with anti-miR-130a or tiny-LNA-130 or relevant matched controls followed by a BrdU pulse for 1h. In both cell types, inhibition of miR-130a alone (anti-miR-130a) decreased BrdU incorporation and thus proliferation. Inhibition of the miR-130/301 family (tiny- LNA-130) led to a greater decrease in proliferation compared with anti-miR-130a, indicating functional redundancy in miR-130/301 family members. **D)** Expression of the proliferation marker PCNA was quantified in PAECs (left panel) and PASMCs (right panel) 48 hours after transfection with miR-130a, anti-miR-130a, tiny-LNA-130 as compared with relevant controls. Correlating with results in **(A, B, C)**, immunoblotting and quantification revealed a modest increase in PCNA expression with miR-130a, a decrease with anti-miR-130a and a more substantial decrease with tiny-LNA-130. In all bar graphs **(A-D)**, data are expressed as mean $\pm$ SD (*P<0.05, ** P<0.01).

Figure S7: siRNA knockdown of PPARγ induces proliferation in PAECs and PASMCs.

A) Exponentially growing cells were transfected with siRNA against PPARγ (si-PPARγ) or control (si-NC) and counted each day for 3 days. Knockdown of PPARγ increased cell number of PAECs (left panel) and PASMCs (right panel) compared with si-NC. **B)** Exponentially growing PAECs (left panel) and PASMCs (right panel) were transfected with si-PPARγ or si-NC and pulsed with BrdU for 1h. Knockdown of PPARγ increased BrdU incorporation and thus proliferation as compared with si-NC. In all panels, data are expressed as mean $\pm$ SD (*P<0.05, ** P<0.01).

Figure S8: Forced expression of PPARγ reverses miR-130a-dependent increases of proliferation.

Forced expression of PPARγ was achieved in PAECs (left panels) and PASMCs (right panels) by lentiviral transduction with a constitutively expressed PPARγ transgene (pPPARγ) that does

not encode for a 3' untranslated region and thus missing the endogenous miR-130/301 binding site. After stable transduction of pPPARγ versus control GFP transgene alone (pGFP), exponentially growing cells were transfected with miR-130a or miR-NC followed by cell counting over three days **(A)** or BrdU pulse-labeling experiments **(B)** as described in Fig. S6-S7. In both cell types transfected with miR-NC, forced expression of PPARγ reduced the level of BrdU incorporation significantly **(B)**, leading to a trend toward decreased cell number **(A)**. Importantly, in both cell types transfected with miR-130a, the miR-130a-induced increases in cell number and BrdU incorporation (miR-130a + pGFP) were significantly reversed (miR-130a + pPPARγ) to baseline levels (miR-NC + pGFP), thus proving the critical importance of PPARγ repression in the proliferative actions of miR-130a. In all panels, data are expressed as mean $\pm$ SD (*P<0.05, ** P<0.01).

Figure S9: The miR-130/301 family does not promote apoptotic signaling in PASMCs during serum starvation.

Exponentially growing PASMCs were transfected with miR-130a, tiny-LNA-130 or matched controls. After two days, cells were serum-starved and assessed for the enzymatic activity of caspases 3/7 as a functional marker of apoptosis. Caspase activity was measured after 24h of serum deprivation. No significant modulation of caspase 3/7 activity was observed in PASMCs grown in serum-replete conditions and transfected with miR-130a or tiny-LNA-130 as compared with control oligonucleotides (miR-NC and tiny-NC, respectively). However, induction of caspase 3/7 activity was observed in PASMCs after 24h of serum deprivation as compared with controls cells (24h starvation). In serum-starved PASMCs, no significant modulation of caspase activity was observed with miR-130/301 manipulation. In all panels, mean levels in control group (miR-NC in serum-replete conditions) were assigned a fold change of 1, to which relevant samples were compared In all panels, data are expressed as mean + SD (*P<0.05, ** P<0.01).

Figure S10: siRNA knockdown of PPARγ mimics the actions of the miR-130/301 family by down-regulating apelin, miR-424, and 503, and up-regulating FGF2 in PAECs.

A-C) Transcript levels of PPARγ (PPARG, left panel-**A**), apelin (APLN, right panel-**A**), and FGF2 **(C)**, as well as expression of miR-424 (left panel-**B**) and miR-503 (right panel-**B**) were quantified in normoxic (21% O_2) PAECs 48h after transfection with siRNA against PPARγ (si-PPARG) or siRNA control (si-NC). RT-qPCR confirmed PPARγ knockdown after treatment with si-PPARγ compared with control (si-NC, left panel-**A**). Under these same conditions, such PPARγ knockdown led to decreased APLN expression (right panel-**A**) as well as decreased miR-424 (left panel-**B**) and miR-503 (right panel-**B**) expression. **C)** Conversely, PPARγ knockdown increased FGF2 transcript levels. **D)** In normoxic PAECs treated with siRNA against PPARγ (PPARγ) or siRNA control (NC), immunoblotting revealed decreased protein levels of PPARγ and apelin but increased FGF2. Actin was used as a loading control. In **(A-C)**, mean levels in control groups exposed to siRNA control (si-NC) were assigned a fold change of 1, to which relevant samples were compared. In all panels, data are expressed as mean $\pm$ SD (*P<0.05, ** P<0.01).

Figure S11: Downstream targets dependent on PPARγ are modulated by miR-130/301 family in both PAECs and PASMCs.

A-D) Transcript levels of PPARγ-dependent targets CCND1, CDKN1A, CDKN2A, and CDKN1B were quantified in PAECs 48h after transfection with **(A)** miR-130a or tiny-LNA-130 versus appropriated controls (miR-NC and tiny-LNA-NC respectively) or **(B)** with siRNA recognizing PPARγ (si-PPARγ) versus siRNA control (si-NC). Consistent with the known regulatory actions of PPARγ on these genes, PPARγ knockdown or miR-130a overexpression decreased CDKN1A, CDKN1B, and CDKN2A expression while increased CCND1 expression as compared

with si-NC control. Conversely, inhibition of miR-130/301 family (tiny-LNA-130) increased CDKN1A, CDKN1B, and CDKN2A expression while decreased CCND1 expression as compared with control (tiny-LNA-NC). **C-D)** In PAECs, forced expression of PPARγ was achieved by lentiviral transduction with a constitutively expressed PPARγ transgene (pPPARγ) that does not encode for a 3' untranslated region and thus missing the endogenous miR-130/301 binding site. Alternatively, pharmacologic activation of PPARγ activity was achieved by 24 h treatment with rosiglitazone (10 μM). In that context, PAECs were transfected with miR-130a or miR-NC. Treatment with rosiglitazone (Rosi) **(C)** or forced expression of PPARγ (pPPARγ) **(D)** reversed the miR-130a-dependent alterations in transcript expression of CCND1, CDKN1A, CDKN2A, and CDKN1B, compared with treatment with rosiglitazone vehicle (DMSO) or transduction with a control transgene (pGFP), respectively. **E-H)** The same experimental approach was performed in PASMCs. **E-F)** As in PAECs, PPARγ knockdown **(F)** or miR-130a overexpression **(E)** decreased CDKN1A, CDKN1B, and CDKN2A expression while increased CCND1 expression as compared with si-NC control. Conversely, inhibition of the miR-130/301 family (tiny-LNA-130) increased CDKN1A, CDKN1B and CDKN2A expression and decreased CCND1 expression as compared with control (tiny-LNA-NC). In PASMCs transfected with miR-130a, pharmacologic activation of PPARγ activity (rosiglitazone 10 μM) **(G)** or forced expression of PPARγ (pPPARγ) **(H)** reversed the miR-130a-dependent alterations in transcript expression of CCND1, CDKN1A, CDKN2A, CDKN1B, compared with treatment with rosiglitazone vehicle (DMSO) or transduction with a control transgene (pGFP). In all panels, mean levels in control groups exposed to miR-NC, tiny-LNA-NC, or siRNA control (si-NC) were assigned a fold change of 1, to which relevant samples were compared. In all panels, data are expressed as mean + SD (*P<0.05, ** P<0.01).

Figure S12: The miR-130/301 family controls the mRNA expression levels of apelin, FGF2, and STAT3.

In normoxia (21% O_2) or hypoxia (0.2% O_2, 24h), either forced expression of miR-130a mimic versus control (miR-NC) or inhibition of miR-130a (anti-miR-130a) versus inhibition of the entire miR-130/301 family (tiny-LNA-130) versus control (anti-miR-NC and tiny-LNA-NC) was performed in cultured PAECs **(A-B)** or PASMCs **(C)**. In PAECs, RT-qPCR revealed that the miR-130/301 family decreased apelin (APLN) **(A)** and increased FGF2 **(B)**. In PASMCs, RT-qPCR revealed that the miR-130/301 family increased STAT3 expression (**C**). In all panels, mean levels in control groups (21% O2 miR-NC or 21% O2 Anti-miR-NC) were assigned a fold change of 1, to which relevant samples were compared. In all panels, data are expressed as mean $\pm$ SD (*P<0.05, ** P<0.01).

Figure S13: Either forced expression of PPARγ or pharmacological activation of PPARγ reverses specific miR-130a-dependent actions in PAECs.

In PAECs, forced expression of PPARγ was achieved by lentiviral transduction with a constitutively expressed PPARγ transgene (pPPARγ) that does not encode for a 3' untranslated region and thus missing the endogenous miR-130/301 binding site. Alternatively, pharmacologic activation of PPARγ activity was achieved by 24 h treatment with rosiglitazone (10 μM). In that context, PAECs were transfected with miR-130a or miR-NC. Forced expression of PPARγ (pPPARγ) or treatment with rosiglitazone (Rosi) reversed the miR-130a-dependent alterations in transcript expression of PPARγ, APLN (**A** and **E**), miR-424 and miR-503 (**B** and **F**), and FGF2 (**C** and **G**) compared with PAECs transduced with a control transgene (pGFP) or treated with rosiglitazone vehicle (DMSO). **D and H)** Under these same conditions, immunoblotting revealed corresponding reversal at the protein level of these miR-130a-dependent alterations in expression. In each panel, identically loaded gels with the same cellular lysates were blotted for

different proteins and the relevant actin loading controls are shown for each gel. In **(A-C)**, mean levels in control groups exposed to pGFP and miR-NC were assigned a fold change of 1, to which relevant samples were compared. In **(E-G)**, mean levels in control groups exposed to DMSO vehicle and miR-NC were assigned a fold change of 1, to which relevant samples were compared. In all histograms, data are expressed as mean ± SD (*P<0.05, ** P<0.01).

Figure S14: Apelin is specifically expressed in PAECs.

Comparison of apelin (APLN) expression by RT-qPCR **(A)** and immunoblotting **(B)** revealed enriched expression in PAECs but not PASMCs. In **(A)**, mean levels in PASMCs were assigned a fold change of 1, to which relevant levels in PAECs were compared. In **(A)**, data are expressed as mean ± SD (*P<0.05, ** P<0.01).

Figure S15: siRNA knockdown of PPARγ mimics the actions of the miR-130/301 family by increasing STAT3 expression as well as decreasing miR-204 in PASMCs.

Transcript levels of PPARγ (PPARγ, left panel-**A**), STAT3 (right panel-**A**), and miR-204 **(B)** were quantified in normoxic (21% O_2) PASMCs 48h after transfection with siRNA against PPARγ (si-PPARγ) or siRNA control. RT-qPCR confirmed PPARγ knockdown after treatment with si-PPARγ (n=3) compared with control (si-NC) (left panel-**A**). Such PPARγ knockdown led to increased STAT3 (right panel-**A**), and decreased miR-204 **(B)**. **C)** Under these same conditions, immunoblotting revealed a corresponding increase in STAT3 expression at the protein level in the context of PPARγ knockdown. In **(A-B)**, mean levels in control groups transfected with si-NC were assigned a fold change of 1, to which relevant samples were compared. In (**A-B**), data are expressed as mean ± SD (*P<0.05, ** P<0.01).

Figure S16: Either forced PPARγ expression or pharmacological activation of PPARγ reverses specific miR-130a-dependent actions in PASMCs.

In PASMCs, forced expression of PPARγ was achieved by lentiviral transduction with a constitutively expressed PPARγ transgene (pPPARγ) that does not encode for a 3' untranslated region and thus missing the endogenous miR-130/301 binding site. Alternatively, pharmacologic activation of PPARγ activity was achieved by 24 h treatment with rosiglitazone (10 μM). In that context, PASMCs were transfected with miR-130a or miR-NC. Forced expression of PPARγ (pPPARγ) or treatment with rosiglitazone (Rosi) reversed the miR-130a-dependent alterations in transcript expression of PPARγ, STAT3 **(A, D)**, and miR-204 (**B, E**) compared with PASMCs transduced with a control transgene (pGFP) or treated with rosiglitazone vehicle (DMSO). **C and F)** Under these same conditions, immunoblotting revealed corresponding reversal at the protein level of these miR-130a-dependent alterations in expression. In **(A-B)**, mean levels in control groups exposed to pGFP and miR-NC were assigned a fold change of 1, to which relevant samples were compared. In **(D-E)**, mean levels in control groups exposed to DMSO vehicle and miR-NC were assigned a fold change of 1, to which relevant samples were compared. In all histograms, data are expressed as mean $\pm$ SD (*P<0.05, ** P<0.01).

Figure S17: Downstream targets of STAT3 are modulated by miR-130/301 in PASMCs.

A-D) Transcript levels of the STAT3 targets NFATC2 and PIM1 were quantified in PASMCs 48h after transfection with **(A)** miR-130a or tiny-LNA-130 versus appropriated controls (miR-NC and tiny-LNA-NC, respectively) or with **(B)** siRNA specific for PPARγ (si-PPARγ) versus siRNA control (si-NC). Consistent with the modulation of STAT3 expression and activity, PPARγ knockdown or miR-130a overexpression increased NFATC2 and PIM1 expression as compared with controls. Conversely, inhibition of the miR-130/301 family (tiny-LNA-130) decreased NFATC2 and PIM1 expression as compared with control (tiny-LNA-NC). **C-D)** In

PASMCs, pharmacologic activation of PPARγ activity was achieved by 24 h treatment with rosiglitazone (10 μM) **(C)**. Forced expression of PPARγ was achieved by lentiviral transduction with a constitutively expressed PPARγ transgene (pPPARγ) **(D)**. Treatment with rosiglitazone (Rosi) or forced expression of PPARγ (pPPARγ) reversed the miR-130a-dependent alterations of NFATC2 and PIM1 as compared with PASMCs treated with rosiglitazone vehicle (DMSO) or transduced with a control transgene (pGFP). In all panels, mean levels in control groups exposed to miR-NC or siRNA control (si-NC) were assigned a fold change of 1, to which relevant samples were compared. In all panels, data are expressed as mean + SD (*P<0.05, ** P<0.01).

Figure S18: Protocol for forced miR-130a expression in the pulmonary tissue and pulmonary vasculature of mice.

In the presence of SU5416 (days of injection are highlighted in red) but in the absence of hypoxia, intrapharyngeal injection of wildtype mice was performed serially 4 times at 1 week intervals with 1nmol of miR-NC or 1nmol of miR-130a (days of administration are in black). During this period, mice were treated daily by oral gavage with 20 mg/kg of rosiglitazone or vehicle. At day 25, echocardiography and right heart catheterization was performed followed by euthanasia and blood/tissue sampling.

Figure S19: Intrapharyngeal injection of miR-130a oligonucleotide is restricted to delivery to the pulmonary tissue and pulmonary vasculature of mice.

A) By RT-qPCR, expression levels of miR-130/301 family members were analyzed in whole lung lysate of mice that underwent serial intrapharyngeal injection of miR-130a or miR-NC oligonucleotides either in the presence or absence of rosiglitazone (n=8 mice/group). Only expression of miR-130a was significantly increased by miR-130a administration. For each

miRNA, mean levels in control groups (miR-NC) were assigned a fold change of 1, to which relevant samples were compared. **B)** Formalin-fixed paraffin-embedded tissue sections of mouse lung treated as (**A**) were analyzed by *in situ* hybridization using probes recognizing miR-130a or scrambled control. Microscopy revealed an increase of staining intensity for miR-130a signal particularly in small pulmonary arterioles. Quantification of staining intensity (right panel) of small pulmonary arterioles (<100 μm diameter, 10 vessels per mouse) revealed significantly and specifically increased miR-130a expression after miR-130a administration. **C)** By RT-qPCR, miR-130a expression was not altered in heart, liver, kidney, or spleen after serial intrapharyngeal administration of either miR-130a or miR-NC in the presence or absence of rosiglitazone (n=7 mice/group). For each organ, mean levels in control groups (miR-NC) were assigned a fold change of 1, to which relevant samples were compared. In all panels, data are expressed as mean ± SEM (*P<0.05, ** P<0.01).

Figure S20: Left ventricular function is unchanged in mice administered miR-130a.

By echocardiography, left ventricular ejection fraction (**A**), fractional shortening (**B**), and interventricular septal thickness at diastole (IVsd, **C**) were unchanged in mice administered miR-130a compared with miR-NC, either in the presence or absence of rosiglitazone (n=8 mice/group). Data are expressed as mean ± SEM (*P<0.05, ** P<0.01).

Figure S21: Forced expression of miR-130a induces PH via at least a partially PPARγ-dependent manner *in vivo.*

A) As assessed by measuring the mass ratio of right ventricle/(left ventricle + septum), right ventricular remodeling was increased by serial intrapharyngeal delivery of miR-130a to mice (miR-130a, n=11 mice) as compared with control (miR-NC, n=13 mice). A non-statistically significant trend toward reversal of such right ventricular pathology was observed with

rosiglitazone treatment (miR-NC + Rosi, n=9 mice; miR-130a + Rosi; n=9). **B)** Pulmonary arteriolar density was assessed in paraffin embedded lung sections after vascular endothelial CD31-staining. The number of vessels (<100μm) was counted in 30 high-power fields (HPF; 400X) per lung, in 8 animals per group. The density of pulmonary arterioles was decreased in mice treated with miR-130a as compared with mice treated with miR-NC. This decrease was reversed by rosiglitazone treatment. **C)** The percentage of muscularized small (<100 μm diameter) pulmonary arterioles in the lungs from mice treated as in (**A)** increased with miR-130a administration. Such remodeling was reversed to baseline levels by rosiglitazone treatment. **D and E)** Confirming the results of Fig. 7D, immunoblotting (**D**) and quantification (**E**) from whole lung lysates revealed decreased PPARγ expression and increased Stat3 phosphorylation in mice administered miR-130a (n=5 mice) compared with miR-NC (n=4 mice). Actin was used as a loading control. Data are expressed as mean ± SEM (*P<0.05, ** P<0.01).

Figure S22: Severity of PH in mice is comparable after either forced expression of miR-130a alone or chronic exposure to hypoxia.

Wildtype mice were exposed to chronic hypoxia (10%O2) for 3 weeks (n=6). In parallel, in the absence of hypoxia, intrapharyngeal injection of wildtype mice was performed serially 4 times at 1 week intervals with 1nmol of miR-NC scrambled control (n=6) or 1nmol of miR-130a (n=8). After 3 weeks, indices of PH were assessed by measuring, right ventricular systolic pressure (RVSP) **(A)**, right ventricular remodeling as reflected by the mass ratio of right ventricle/(left ventricle + septum) **(B)**, the density of pulmonary arterioles **(C)**, pulmonary arteriolar remodeling [via immunohistochemical (IHC) staining of <100μm diameter pulmonary vessels for α-smooth muscle actin (α-SMA)] **(D)**, and the percentage of muscularized small (100<μm diameter) pulmonary arterioles **(E)**. Both hypoxia and miR-130a similarly increased RVSP **(A)**, ventricular remodeling **(B),** pulmonary arterioles remodeling **(D)**, and the percentage of muscularized small

pulmonary arterioles **(E)**. Conversely, both hypoxia and miR-130a similarly decreased the density of pulmonary arterioles **(C)** compared with controls (normoxia (21% O2; n=6) and administration of miR-NC, respectively). Data are expressed as mean ± SEM (*P<0.05, ** P<0.01). Scale bar 50µm.

Figure S23: Protocol for pharmacologic inhibition of the miR-130/301 family in the pulmonary tissue and pulmonary vasculature of mice in order to reverse PH progression *in vivo*. Wildtype mice were exposed to chronic hypoxia + SU5416. After two weeks of exposure and confirmation of PH by increased RVSP (Ctrl 2 weeks, n=5 mice), exposure to chronic hypoxia + SU5416 was continued in a separate cohort of mice for another 2 weeks, accompanied by serial intrapharyngeal injections (every 4 days for a total of 3 doses) with 10mg/kg of control oligonucleotide (Short-NC, n=7 mice), "shortmer" oligonucleotide recognizing the seed sequence of the miR-130/301 family (Short-130, n=7 mice), or PBS (n=4 mice).

Figure S24: Intrapharyngeal injections of shortmers are restricted to delivery to the pulmonary tissue and pulmonary vasculature of mice.

A) Intrapharyngeal injections of Cy5-labeled tiny-oligonucleotide (10 mg/kg) were performed in mice (n=10 mice). After two days, mice were euthanized and cryosections were obtained from from lung, heart and liver. Vascular endothelium was identified by anti-CD31 staining (green), and Cy5-labeled shortmer was localized by red stain. Delivery of shortmer was confirmed specifically in pulmonary vessels of the lung but not the heart or liver. **B)** To directly assess the localization of the delivered oligonucleotide in the lung of injected mice, antibodies were developed recognizing the oligonucleotide modifications in the shortmer backbone (see **Methods**). Immunohistochemistry (IHC) of three serial sections of mouse lung injected with PBS (n=4) or Short-130 (n=7) were performed using antibody against α-SMA (smooth muscle cells), CD31 (endothelial cells) and shortmer oligonucleotide (Short-130). Shortmer

oligonucletide labeling revealed that Short-130 appears to localize in both endothelial and smooth muscle cells. Scale bar 50μm.

Figure S25: Left ventricular function is unchanged in mice administered Short-130.

By echocardiography, left ventricular ejection fraction **(A)**, fractional shortening **(B)**, and interventricular septal thickness at diastole (IVsd) **(C)** were unchanged in mice exposed to hypoxia + SU5416 (4 weeks) and administered Short-130 compared with Short-NC (n=5 mice/group). Data are expressed as mean ± SEM (*P<0.05, ** P<0.01).

Figure S26: Inhibition of the miR-130/301 family by Short-130 reverses multiple molecular, histologic, and hemodynamic indices of experimental PH in mice *in vivo*.

A) In the context of pre-existing PH in mice caused by chronic hypoxia + SU5416, as assessed by measuring the mass ratio of right ventricle/(left ventricle + septum), right ventricular remodeling was decreased by serial intrapharyngeal delivery of Short-130 (n=7 mice) as compared with control (Short-NC; n=7 mice) or PBS treatment (PBS; n=4 mice) where right ventricular remodeling increased over time. **B)** The density of pulmonary arterioles progressively decreased after two weeks (Ctrl 2 weeks) and four weeks of hypoxia+SU5416 exposure (Short-NC) as compared with control mice (normoxia +SU5416). Treatment with Short-130 prevented the decline of pulmonary arteriolar density as compared with control (Short-NC). **C)** The percentage of muscularized small (100<μm diameter) pulmonary arterioles in the lungs from mice treated as in (**A)** decreased with Short-130 administration (n=7 mice) as compared with control (Short-NC; n=7 mice), where arteriolar muscularization increased over time. **D)** Confirming the results of Fig. 8D, immunoblotting (left panel) and quantification (right panel) from whole lung lysates revealed increased PPARγ expression and decreased Stat3 phosphorylation in mice administered Short-130a (n=5 mice) compared with Short-NC (n=4

mice). Actin was used as a loading control. Data are expressed as mean ± SEM (*P<0.05, ** P<0.01).

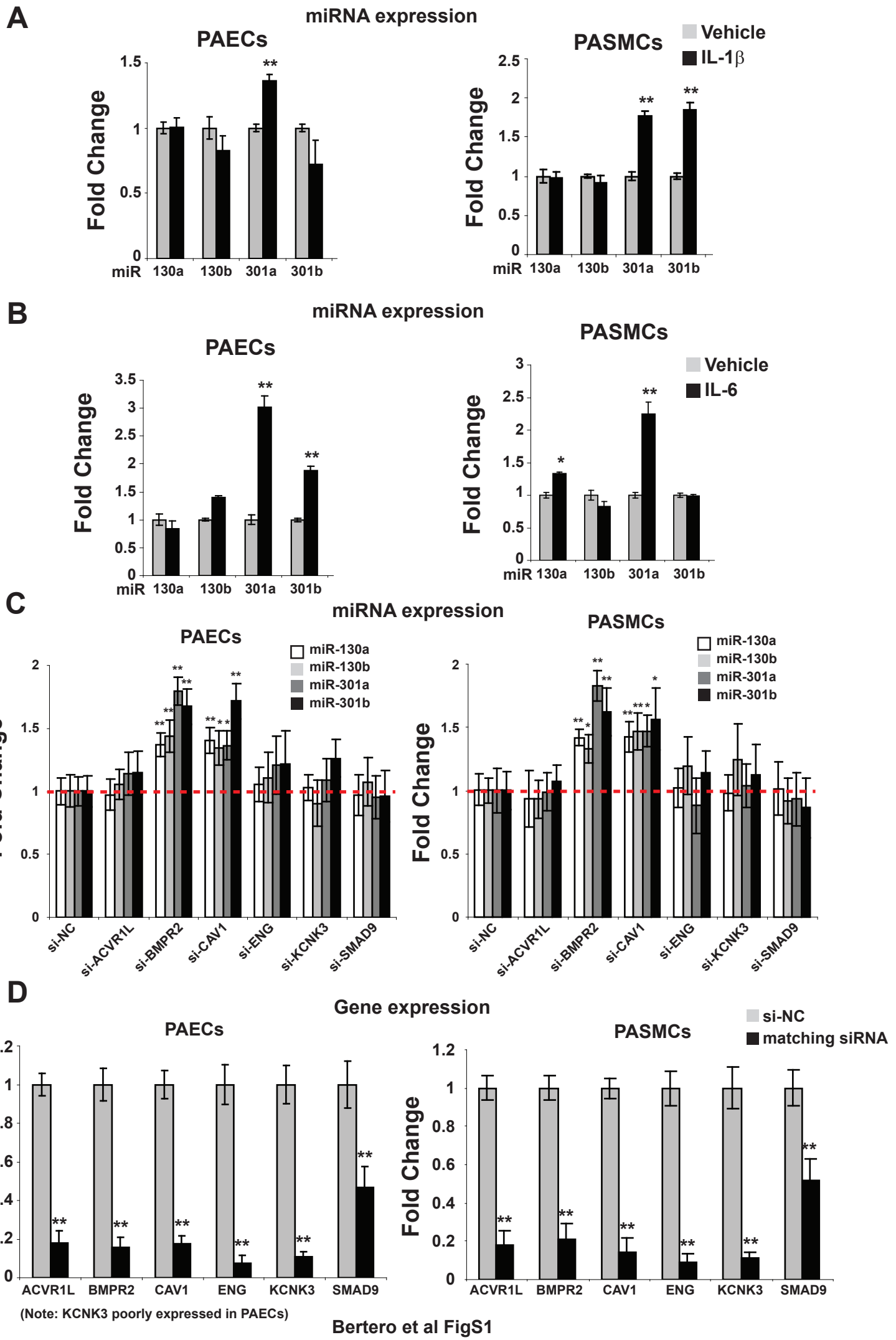
A
miRNA expression
PAECs
PASMCs
Vehicle
IL-1β
Fold Change
miR 130a 130b 301a 301b
B
miRNA expression
PAECs
PASMCs
Vehicle
IL-6
Fold Change
miR 130a 130b 301a 301b
C
miRNA expression
PAECs
PASMCs
miR-130a
miR-130b
miR-301a
miR-301b
Fold Change
si-NC
si-ACVR1L
si-BMPR2
si-CAV1
si-ENG
si-KCNK3
si-SMAD9
D
Gene expression
PAECs
PASMCs
si-NC
matching siRNA
Fold Change
ACVR1L BMPR2 CAV1 ENG KCNK3 SMAD9
(Note: KCNK3 poorly expressed in PAECs)
Bertero et al FigS1

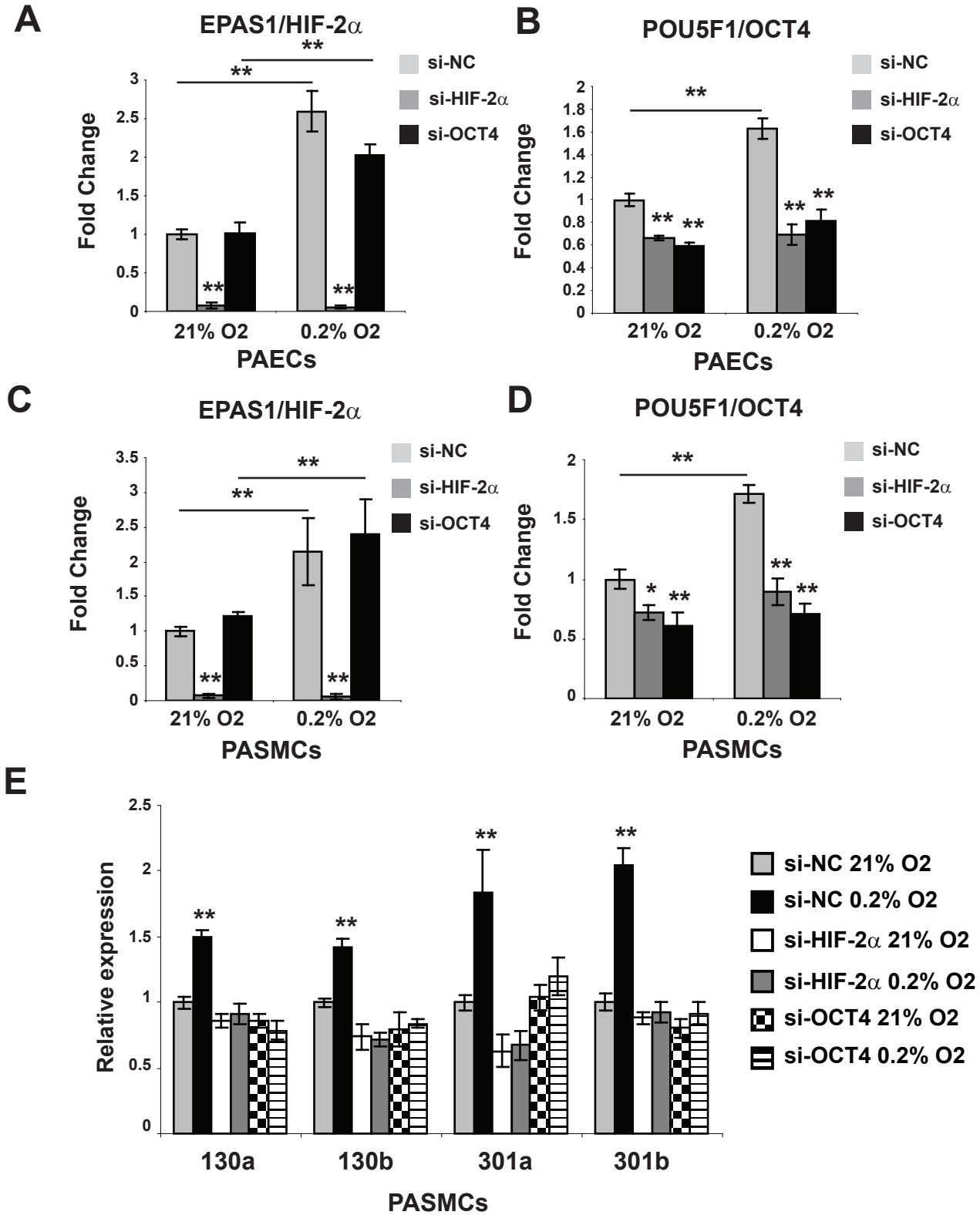

Bertero et al FigS2

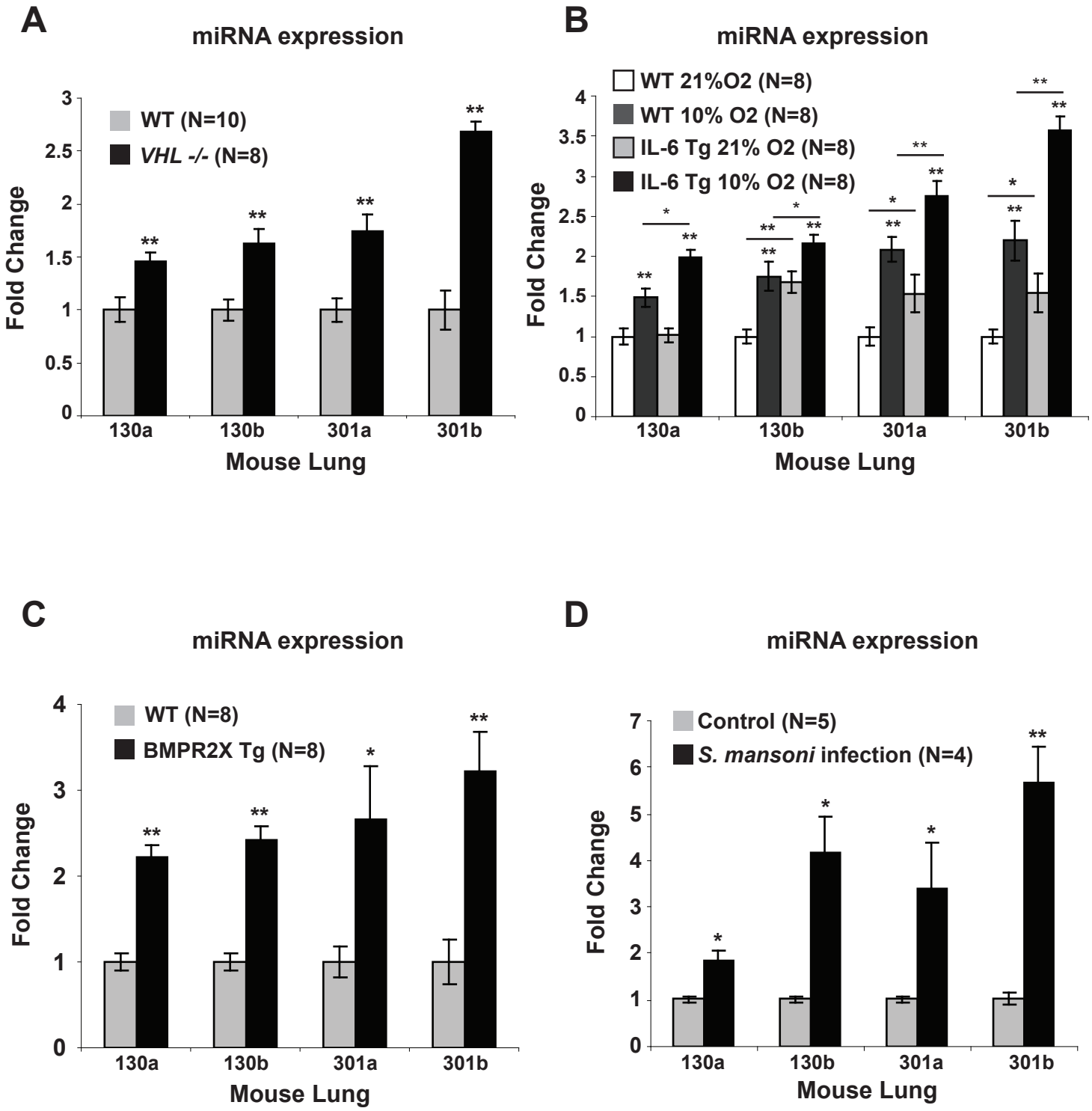

Bertero et al FigS3

A

3'UTR of PPARγ

```
Hsa CCCUUCUUCCAGUUGCAC---UAUUCUG
Mmu UCCUUCUAUUGAUUGCACUAUUAUUUUG
Rno UCCUUCUAUCGAUUGCACUAUUAUUUUG
Dno UCCUCCUCCCAGUUGCACUAUUAUUUUG
Xtr ACUCGCCCCCAUUUGCACUAUUUCUAUA
                  | | | | | | |
    UACGGGAAAAUUGUAACGUGAC hsa-miR-130a
```

B

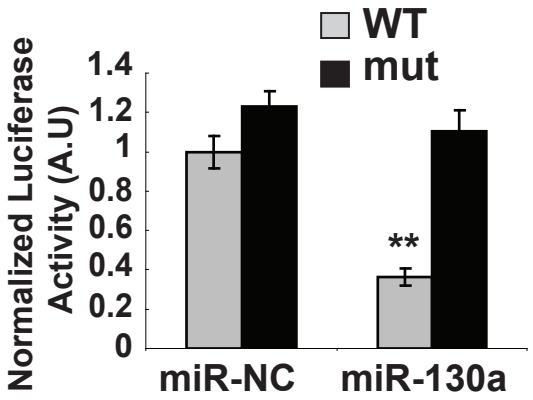

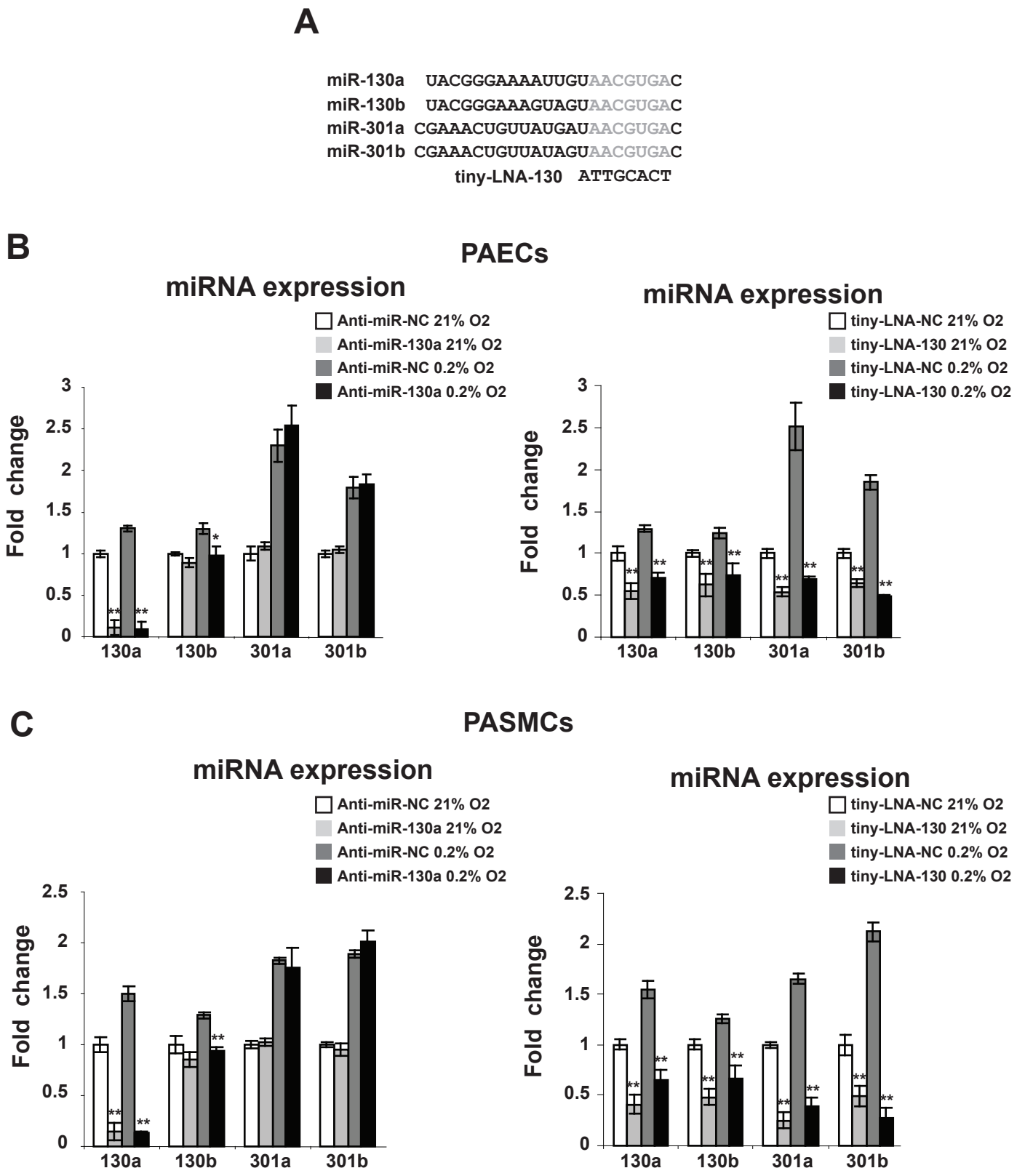

Bertero et al FigS5

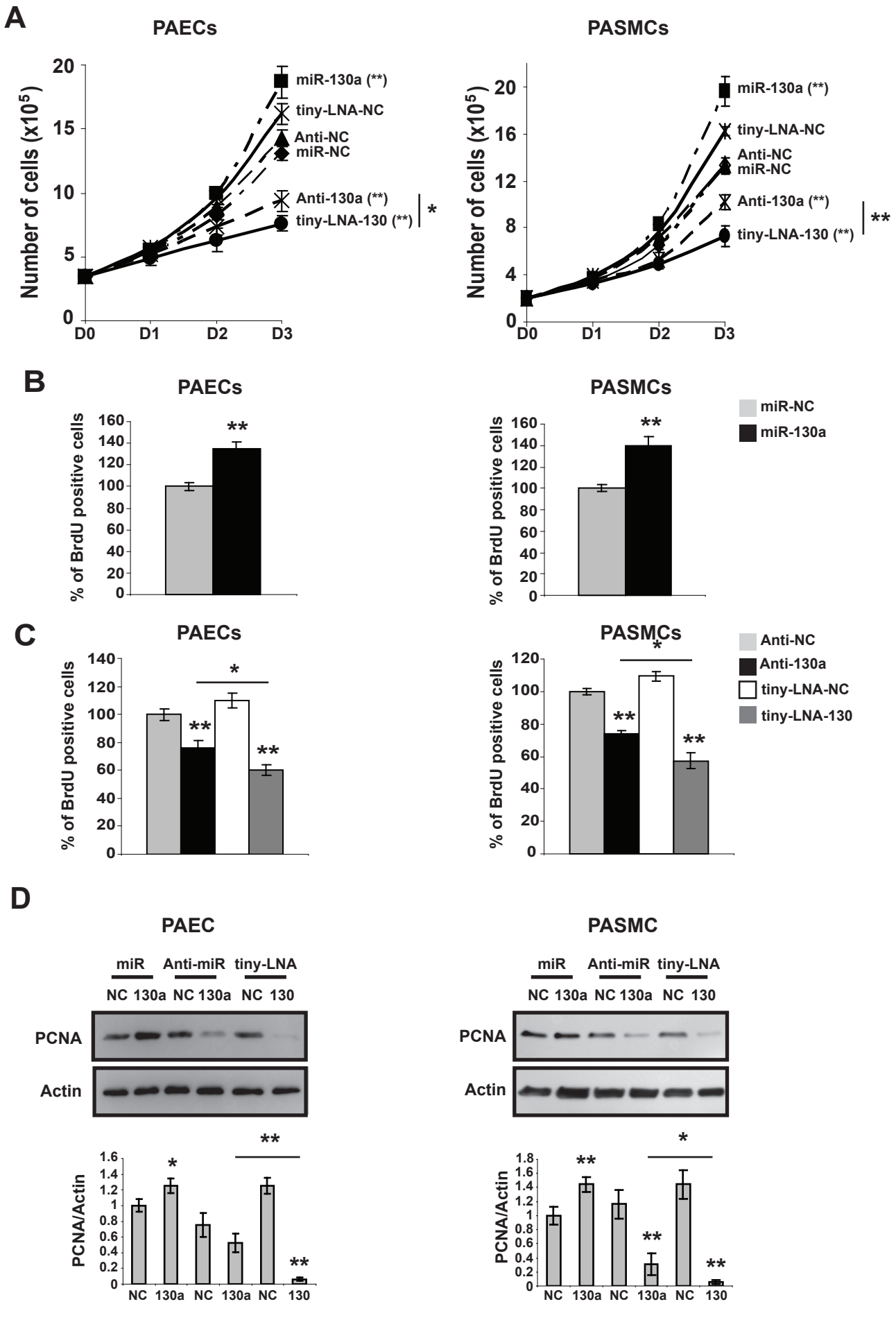

Bertero et al FigS6

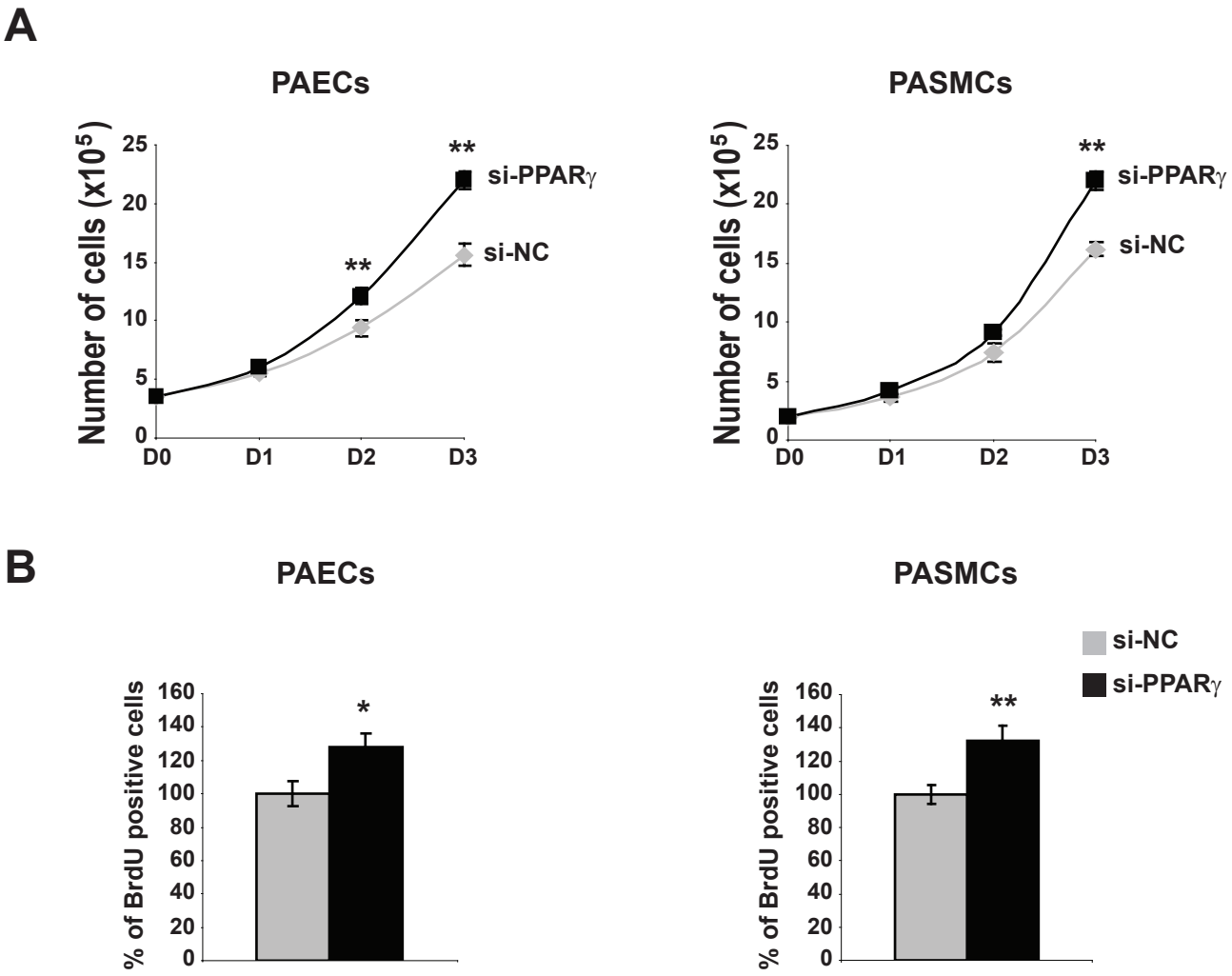

Bertero et al FigS7

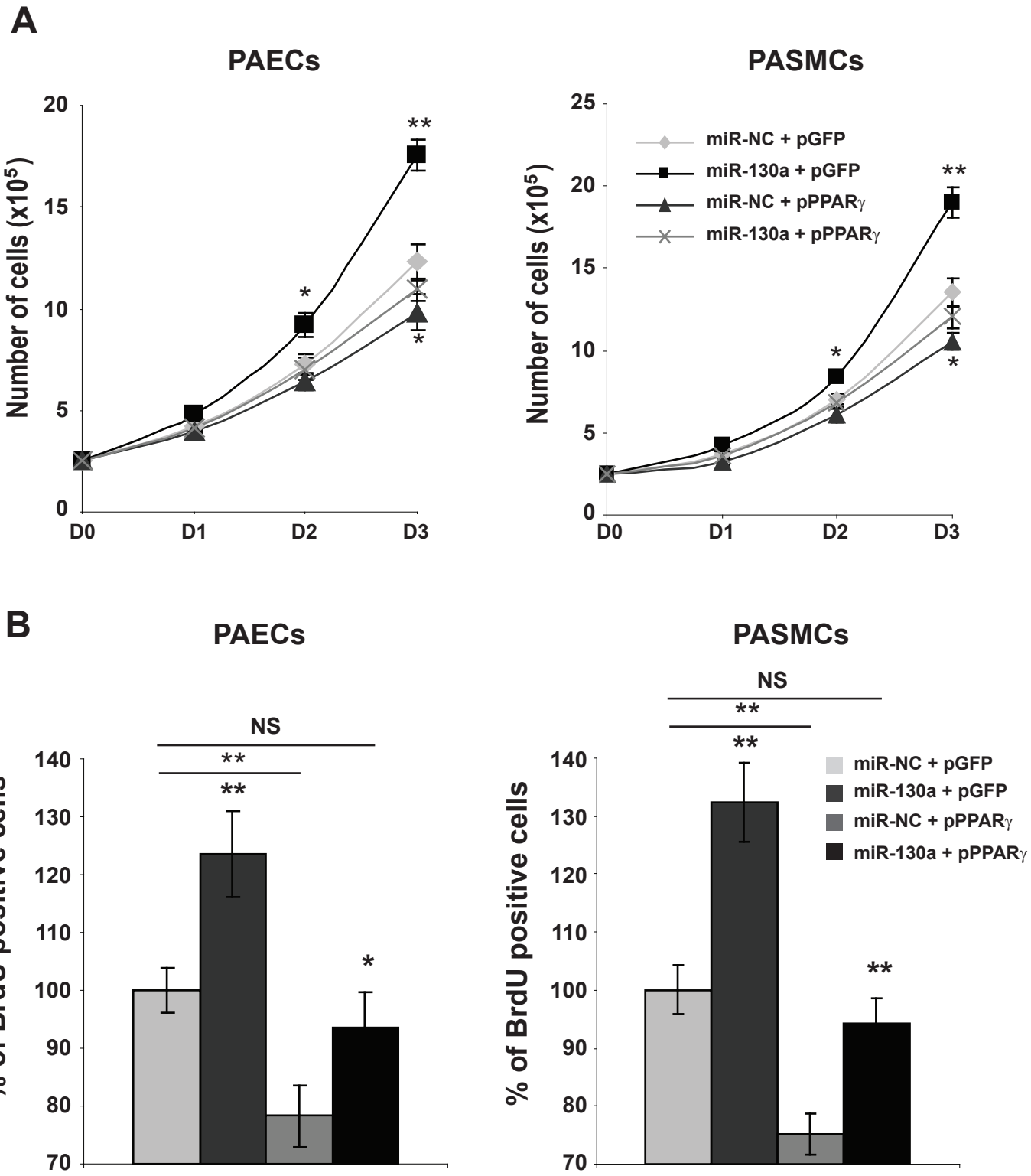

Bertero et al FigS8

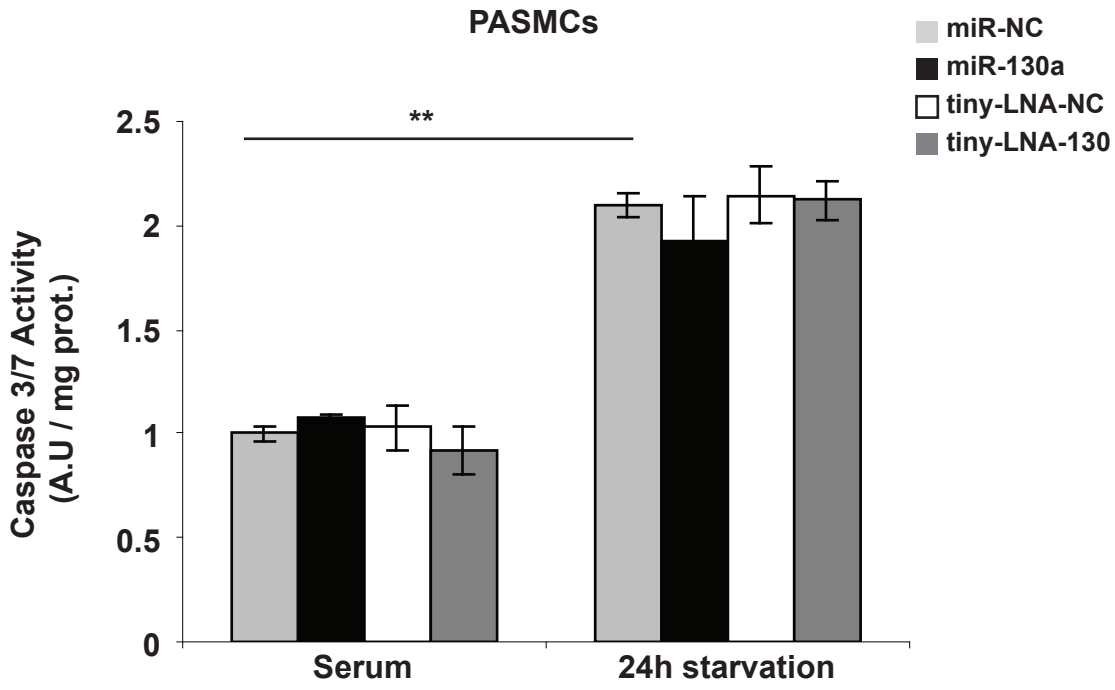

Bertero et al. FigS9

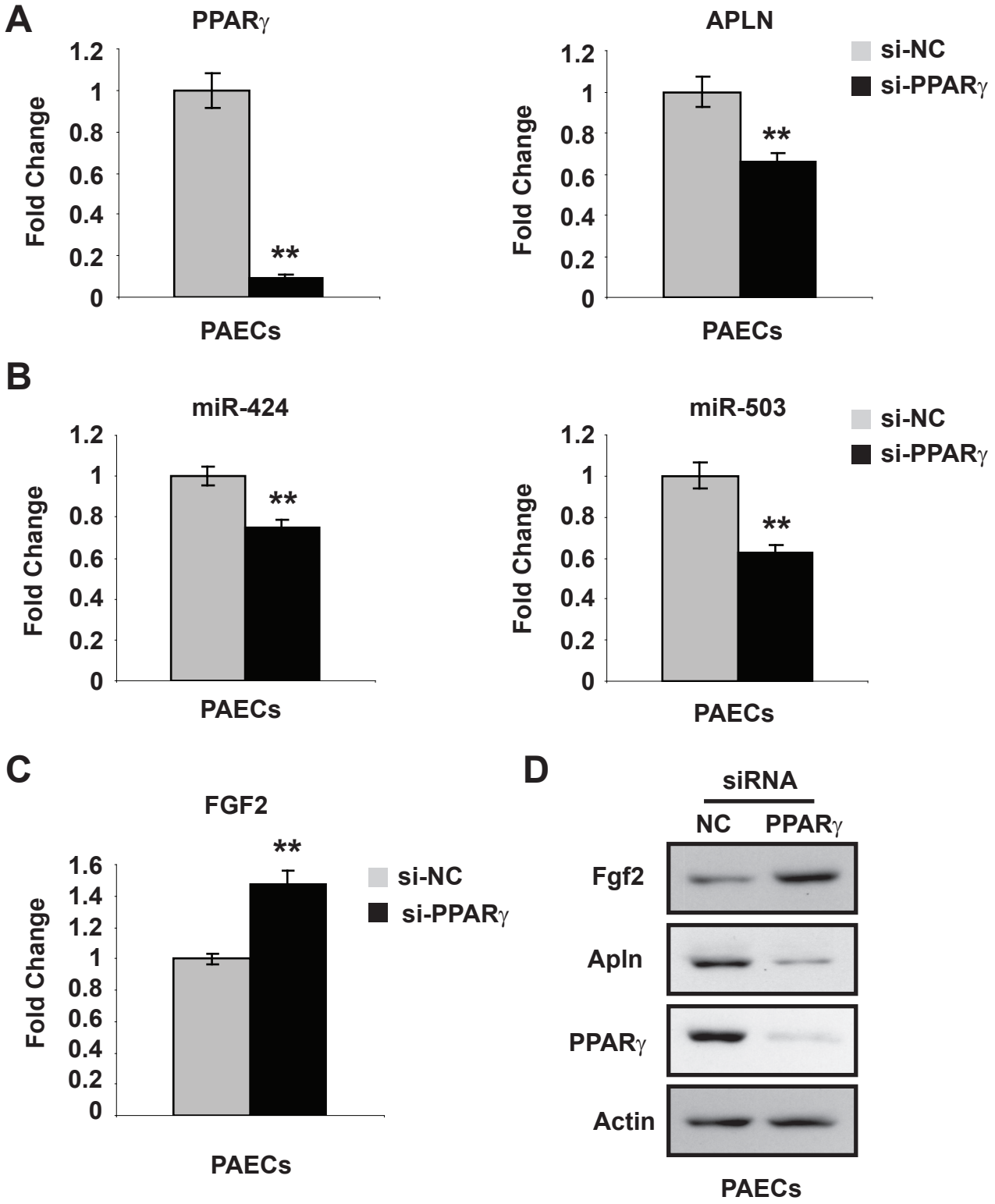

Bertero et al FigS10

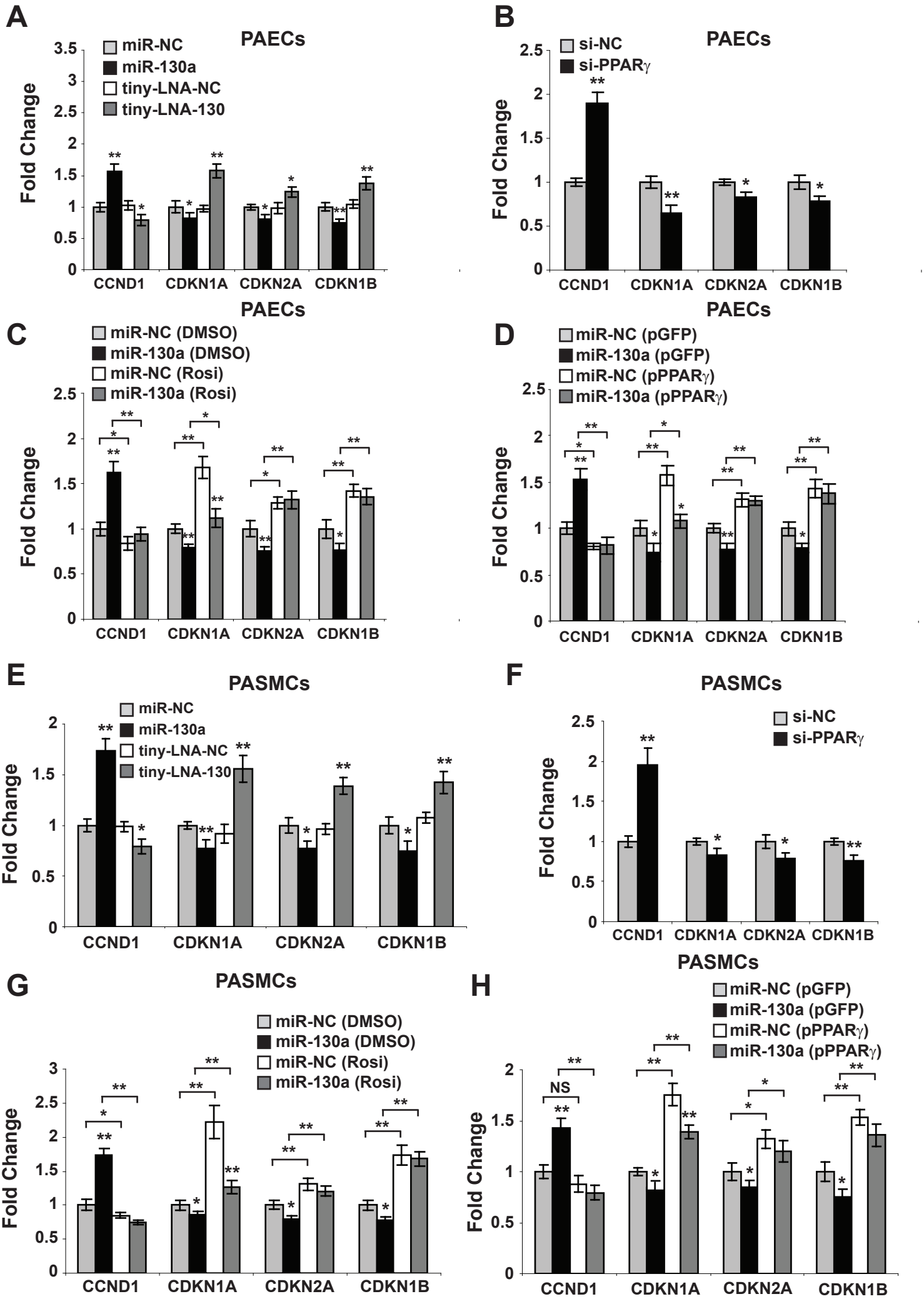

Bertero et al FigS11

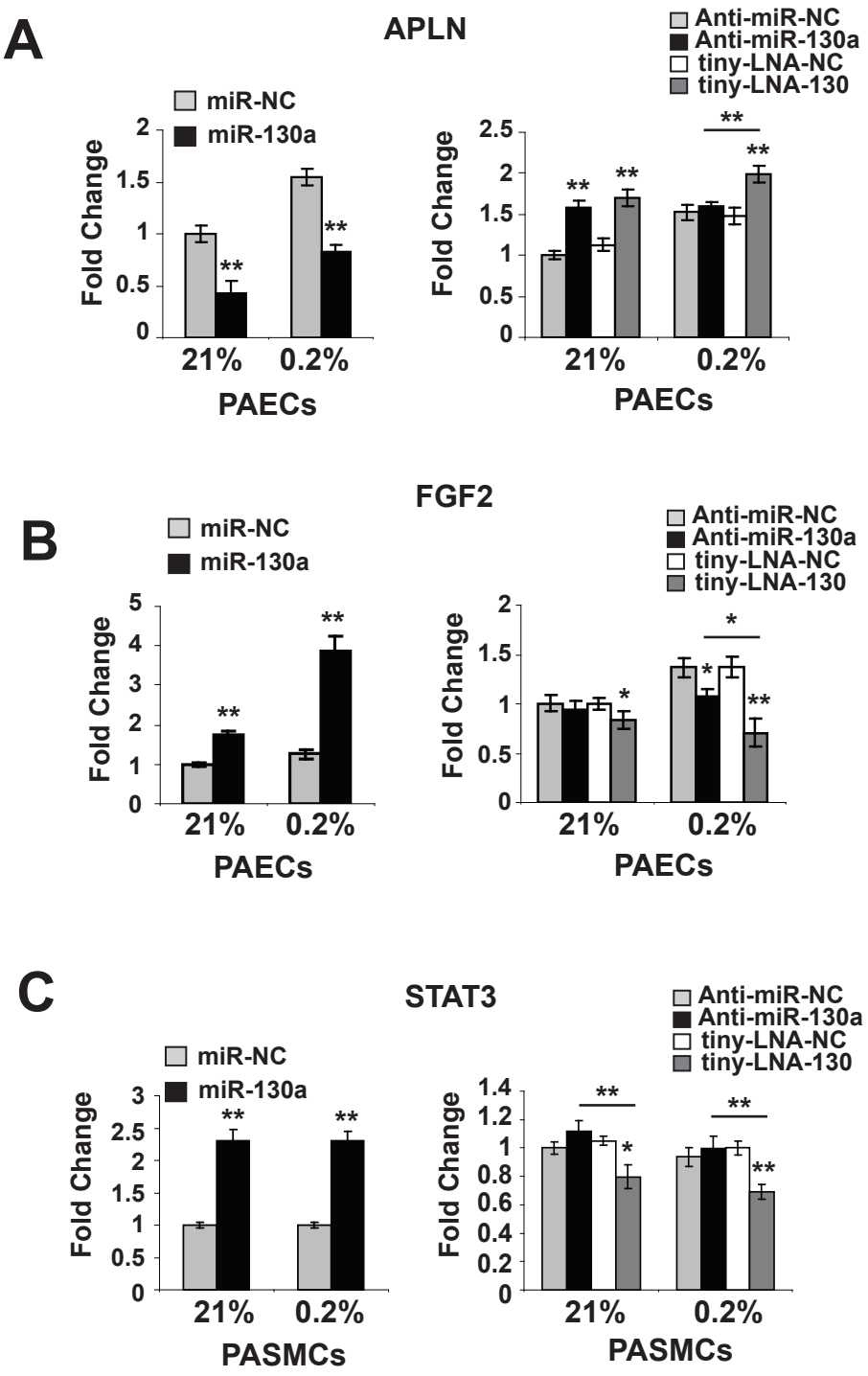

Bertero et al FigS12

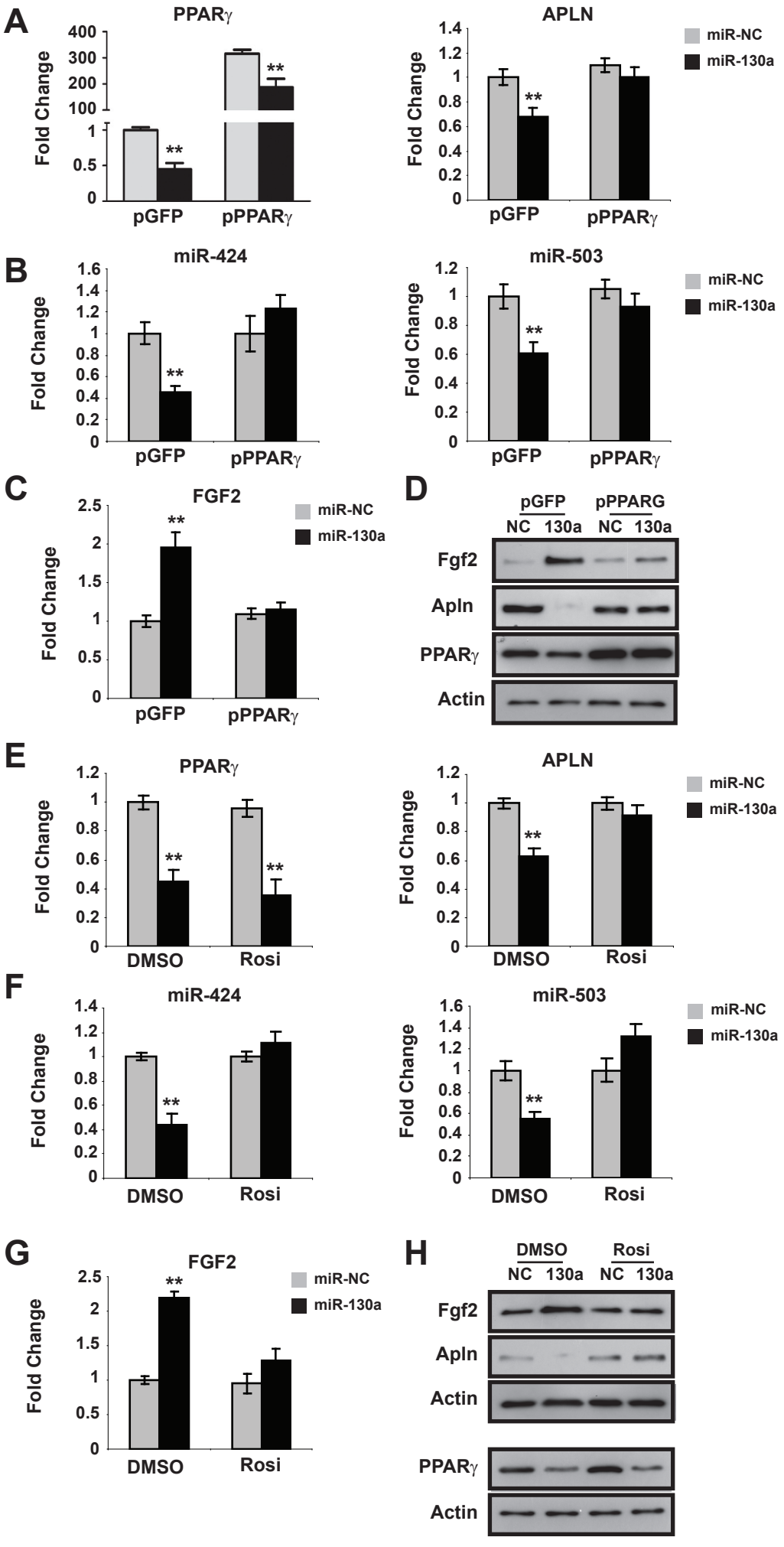

Bertero et al FigS13

A

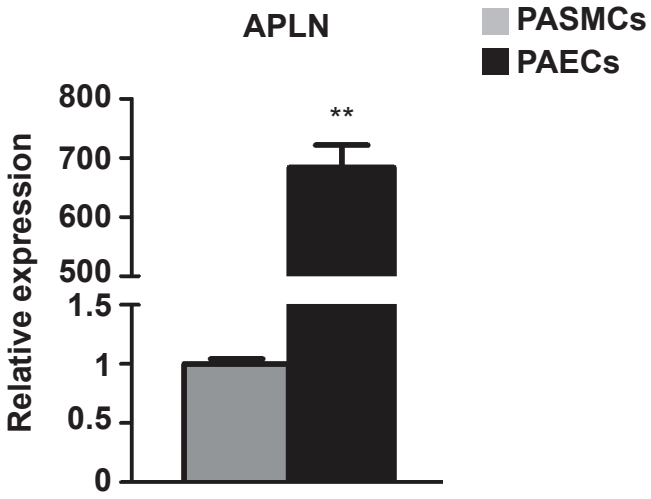

B

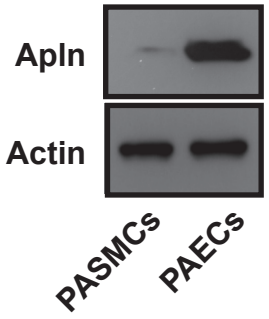

Bertero et al FigS14

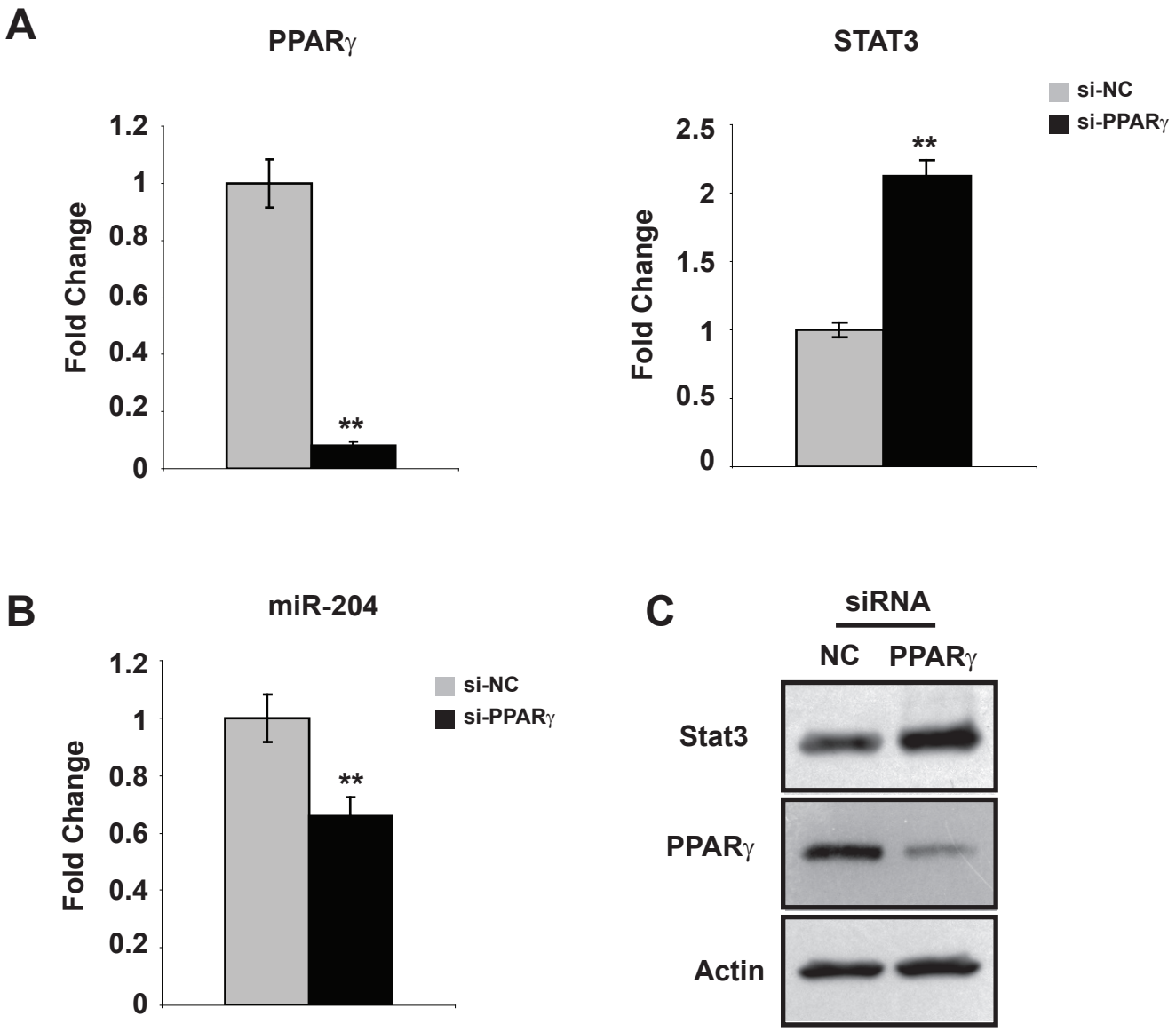

Bertero et al FigS15

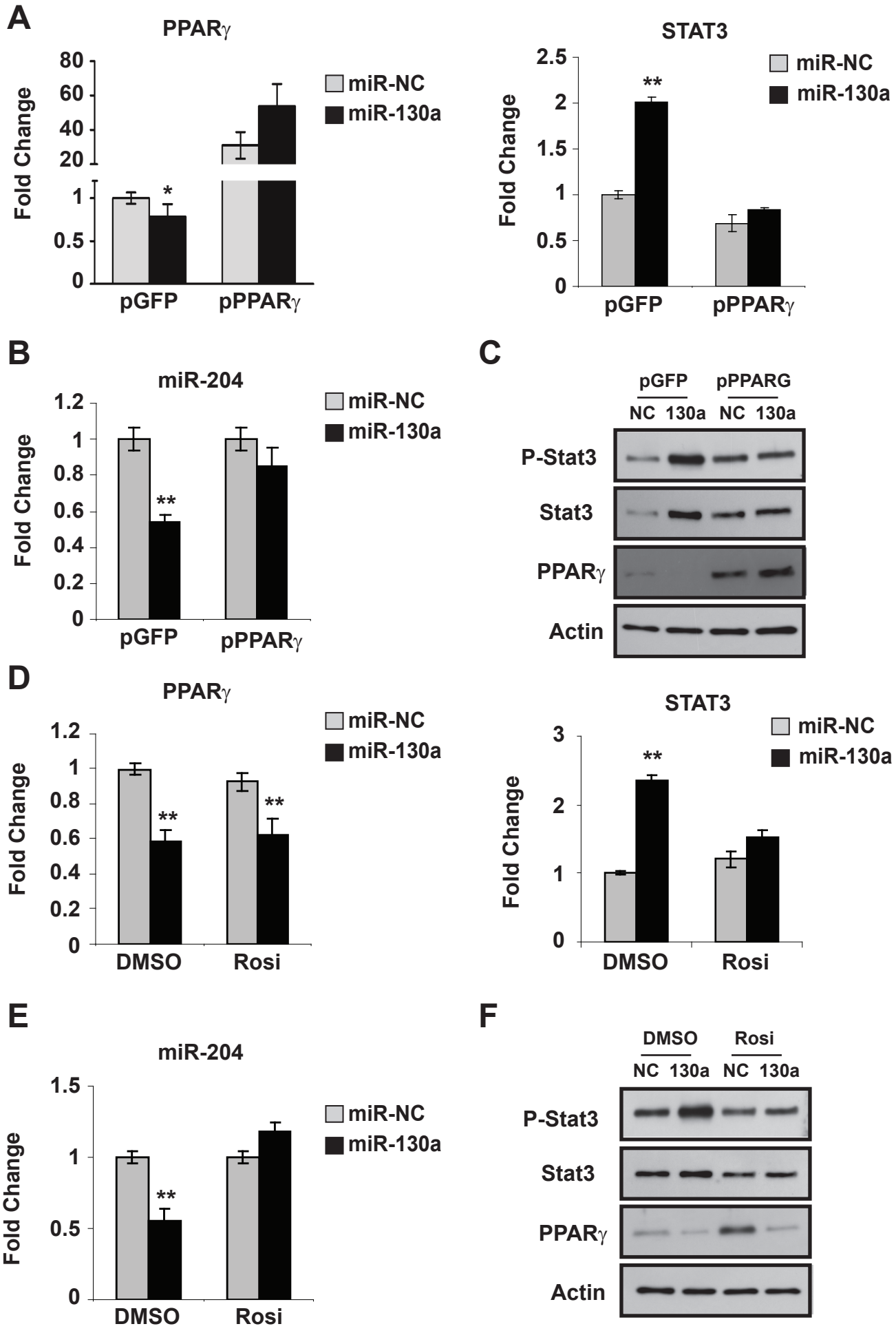

Bertero et al FigS16

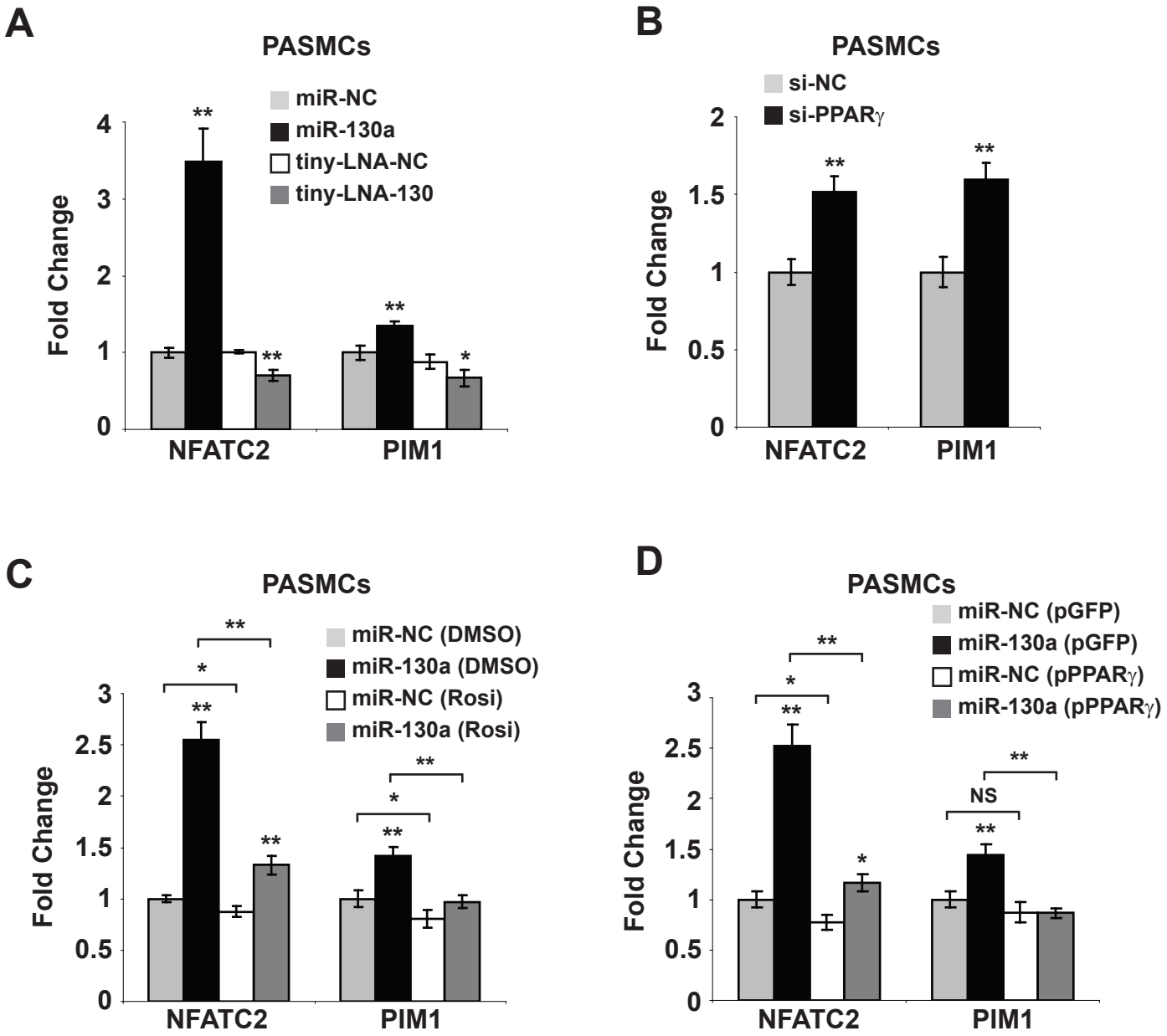

Bertero et al FigS17

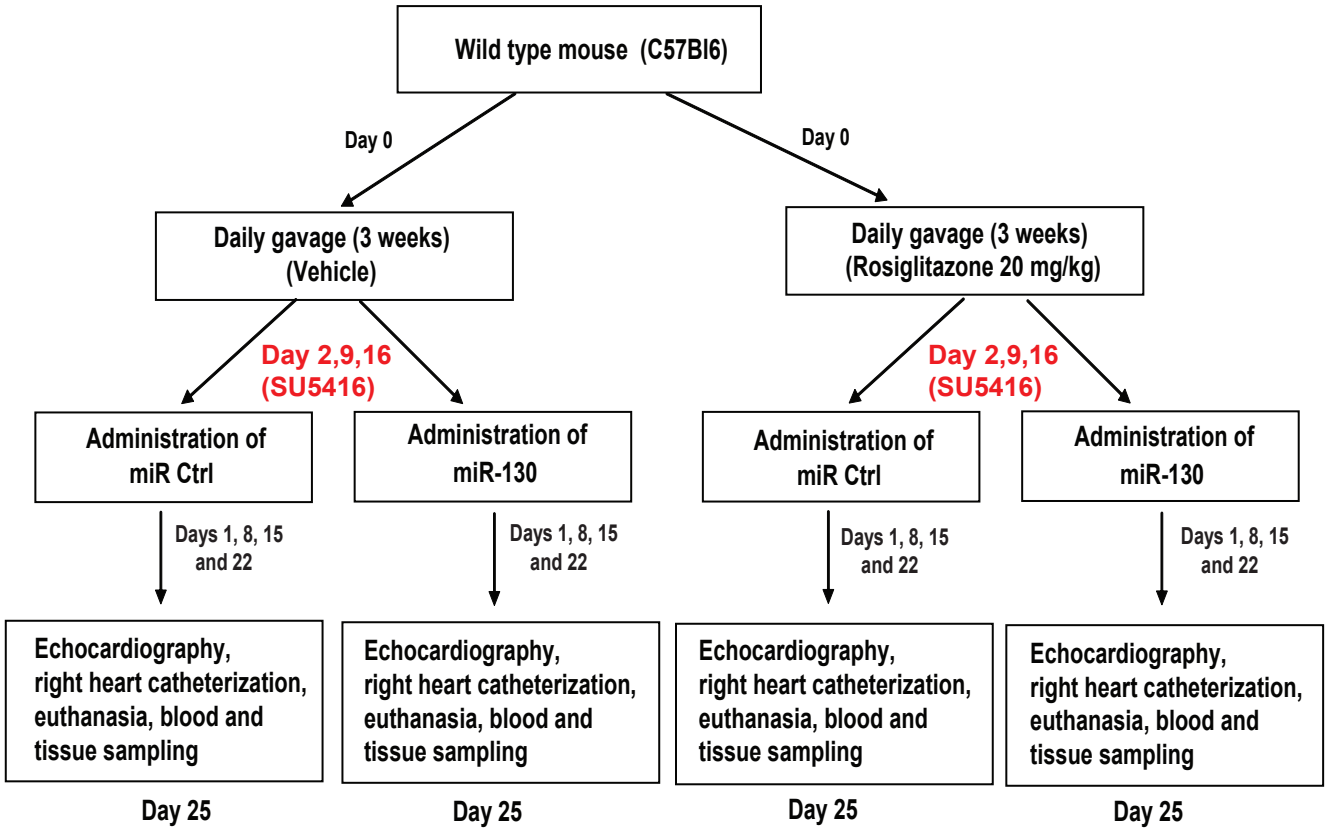

Bertero et al FigS18

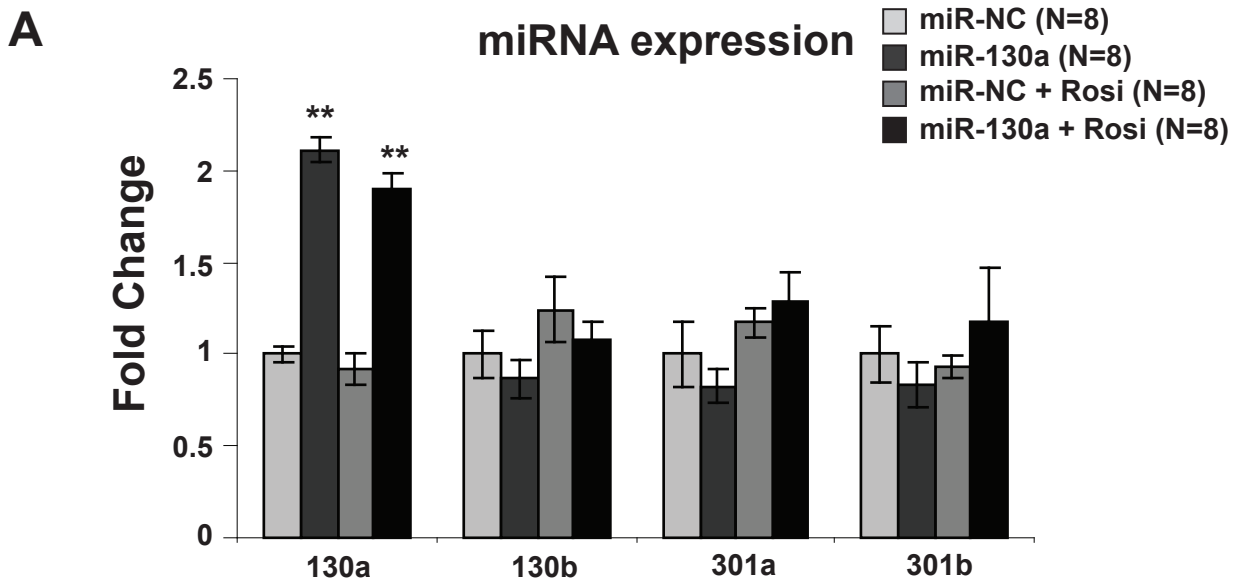

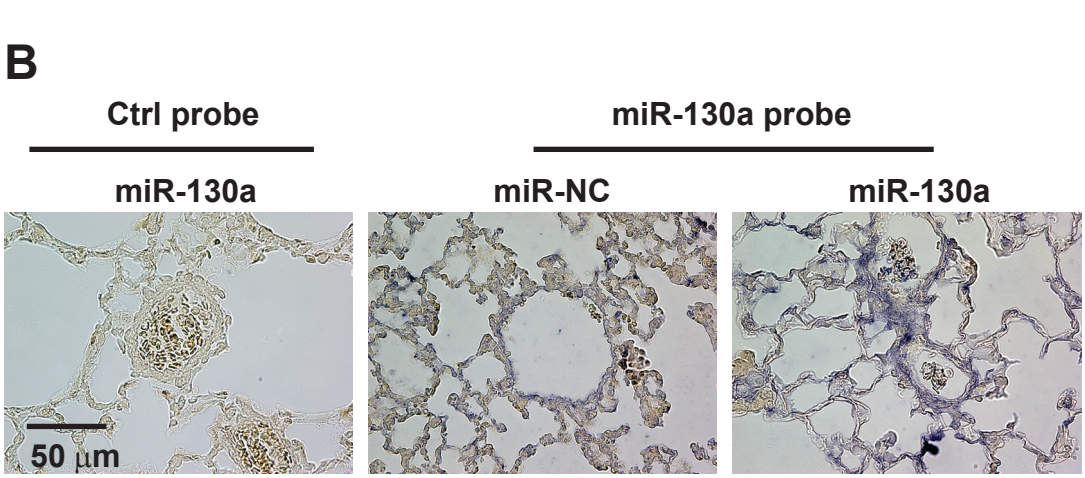

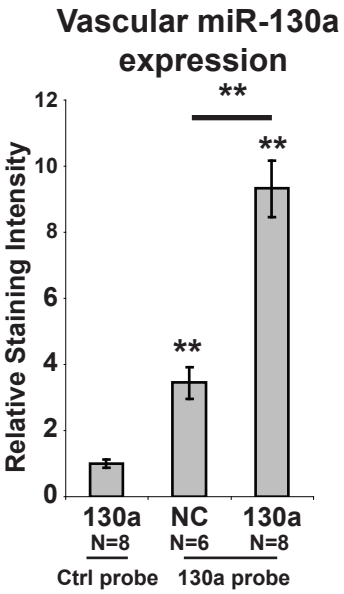

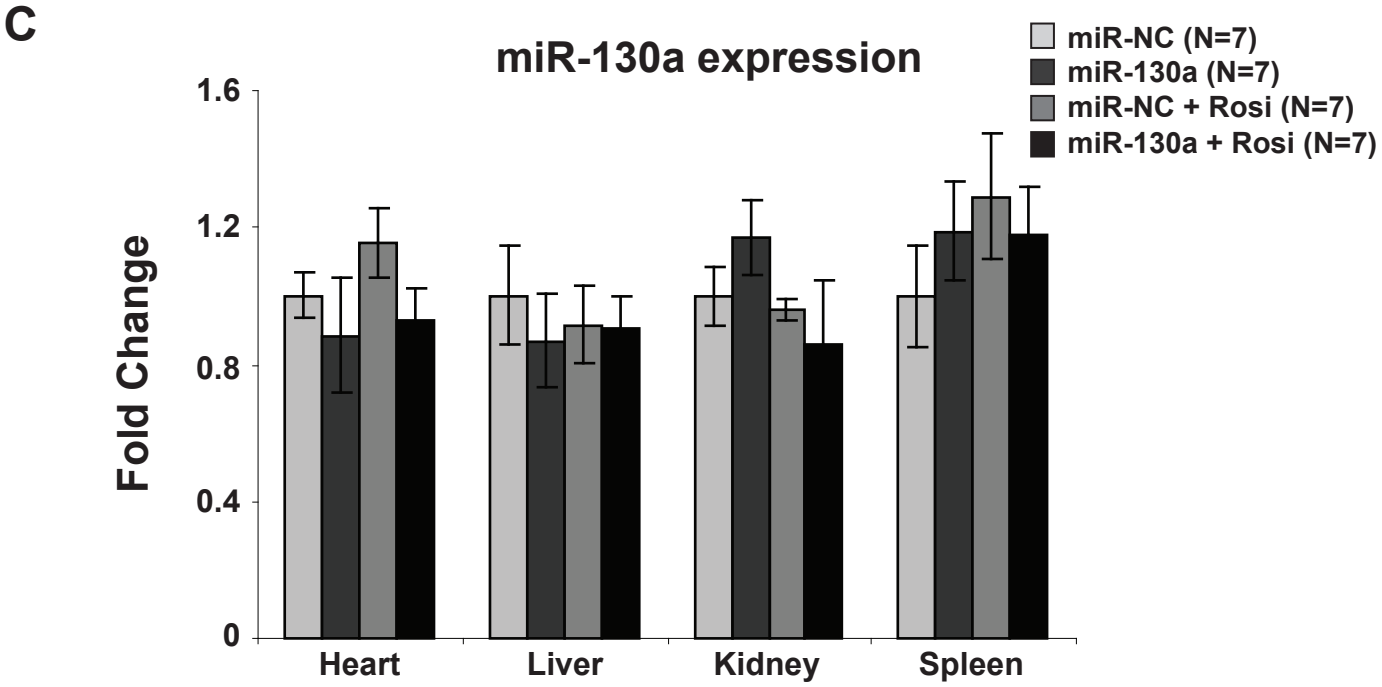

Bertero et al FigS19

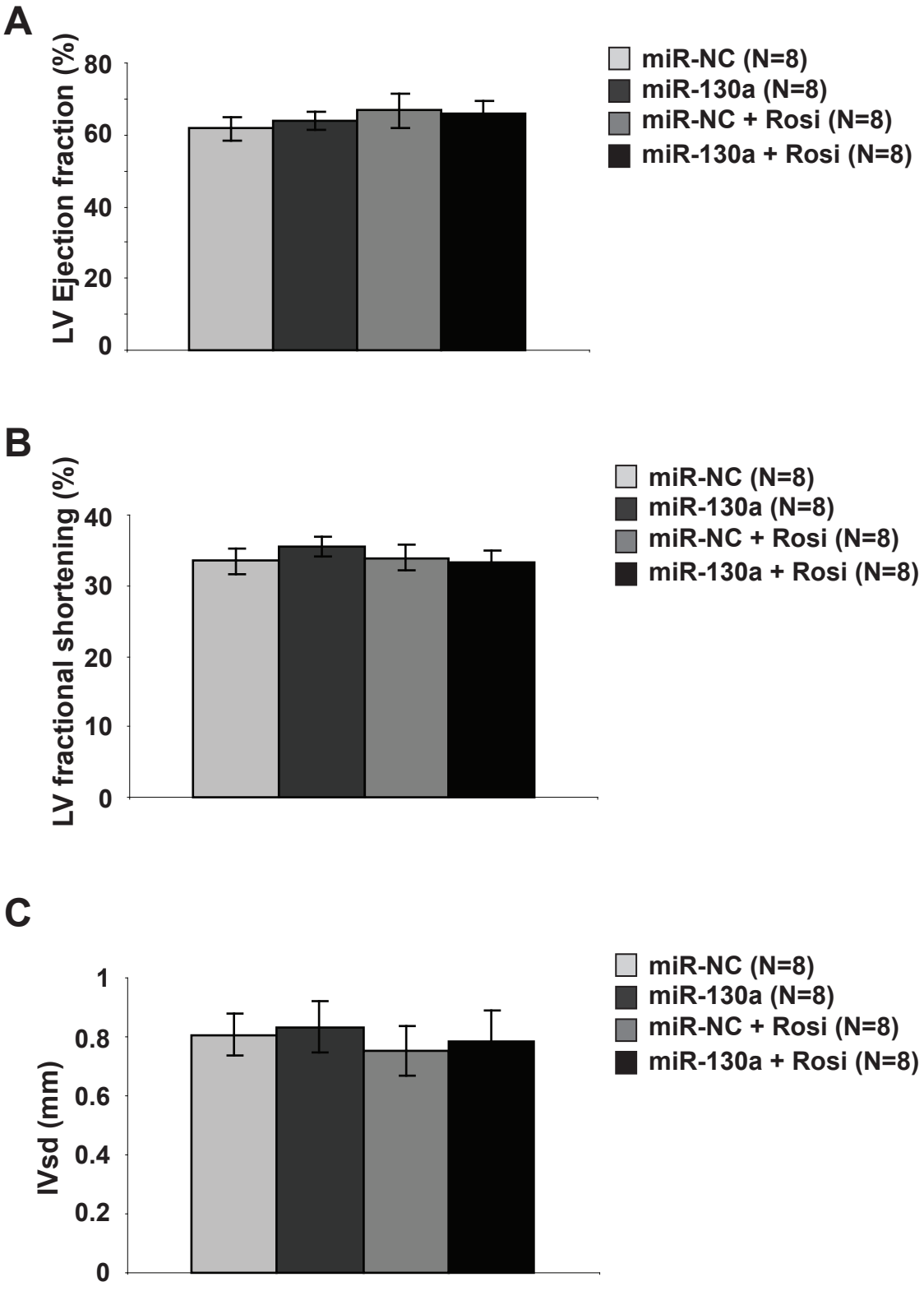

Bertero et al FigS20

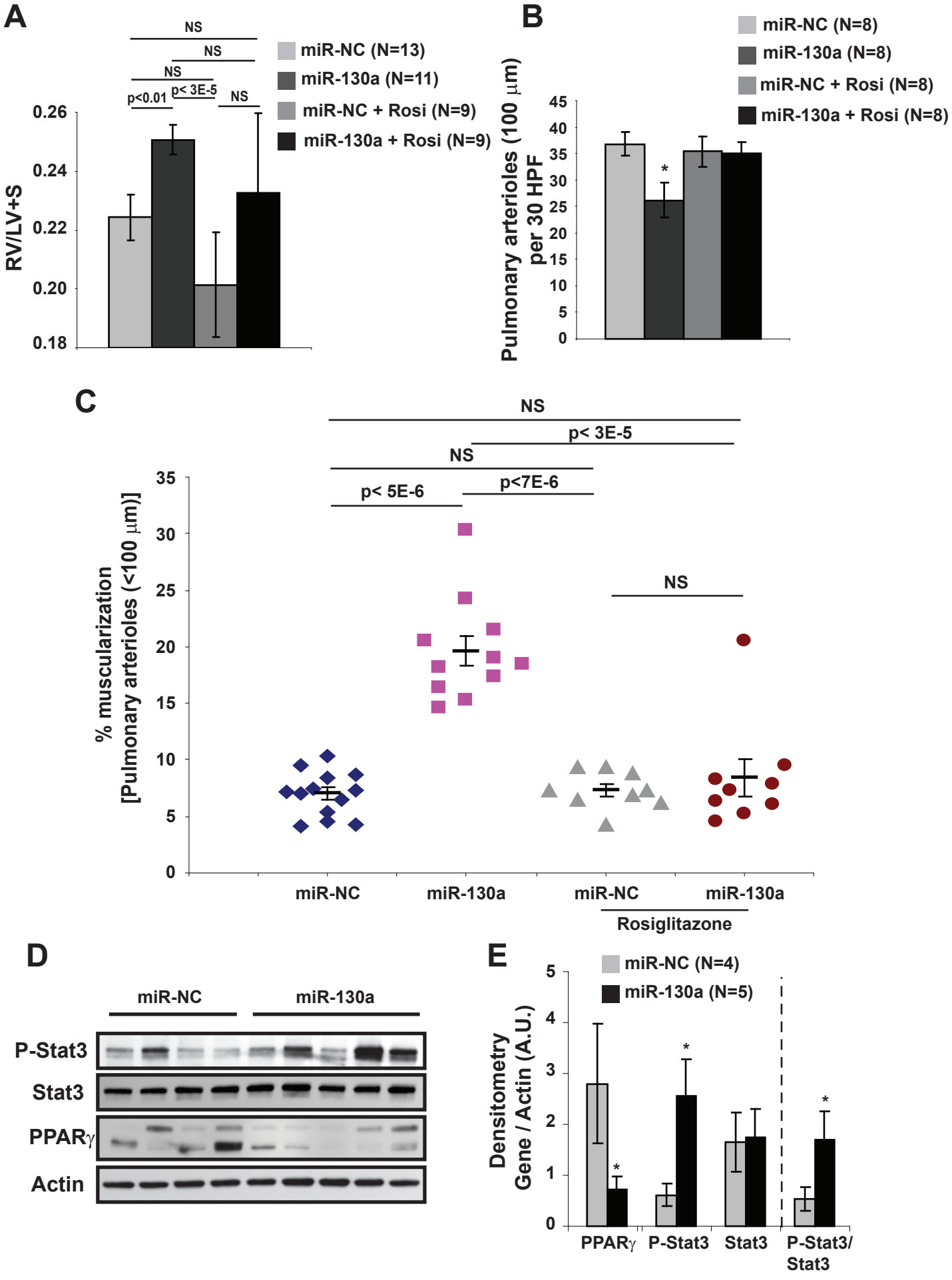

Bertero et al FigS21

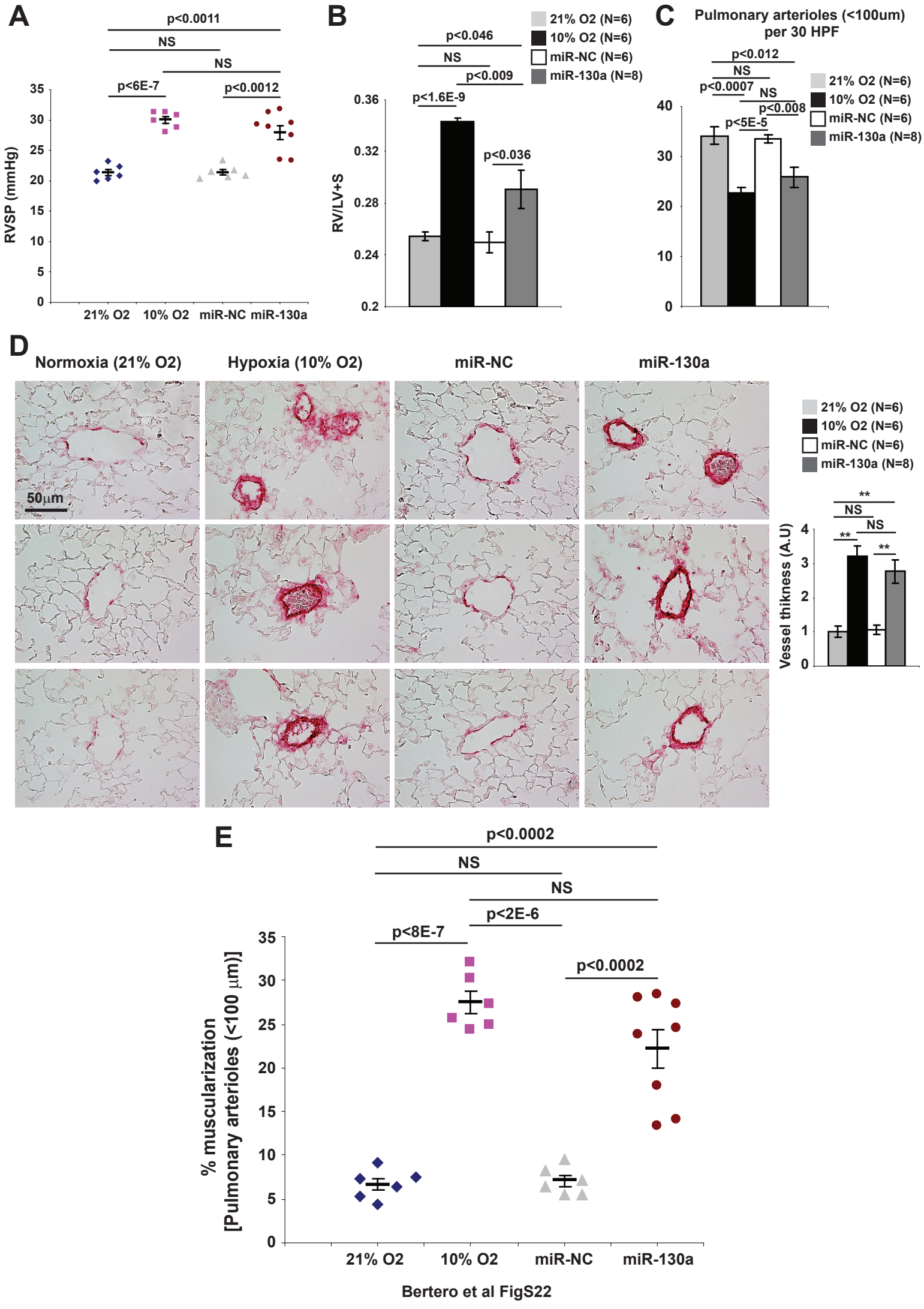
A
p<0.0011
NS
NS
p<6E-7
p<0.0012
RVSP (mmHg)
35
30
25
20
15
10
5
0
21% O2
10% O2
miR-NC
miR-130a
B
21% O2 (N=6)
10% O2 (N=6)
miR-NC (N=6)
miR-130a (N=8)
p<0.046
NS
p<0.009
p<1.6E-9
p<0.036
RV/LV+S
0.36
0.32
0.28
0.24
0.2
C
Pulmonary arterioles (<100um) per 30 HPF
p<0.012
NS
p<0.0007
NS
p<0.008
p<5E-5
40
30
20
10
0
21% O2 (N=6)
10% O2 (N=6)
miR-NC (N=6)
miR-130a (N=8)
D
Normoxia (21% O2)
Hypoxia (10% O2)
miR-NC
miR-130a
50μm
21% O2 (N=6)
10% O2 (N=6)
miR-NC (N=6)
miR-130a (N=8)
**
NS
NS
**
**
Vessel thikness (A.U)
4
3
2
1
0
E
p<0.0002
NS
NS
p<2E-6
p<8E-7
p<0.0002
% muscularization [Pulmonary arterioles (<100 μm)]
35
30
25
20
15
10
5
0
21% O2
10% O2
miR-NC
miR-130a
Bertero et al FigS22

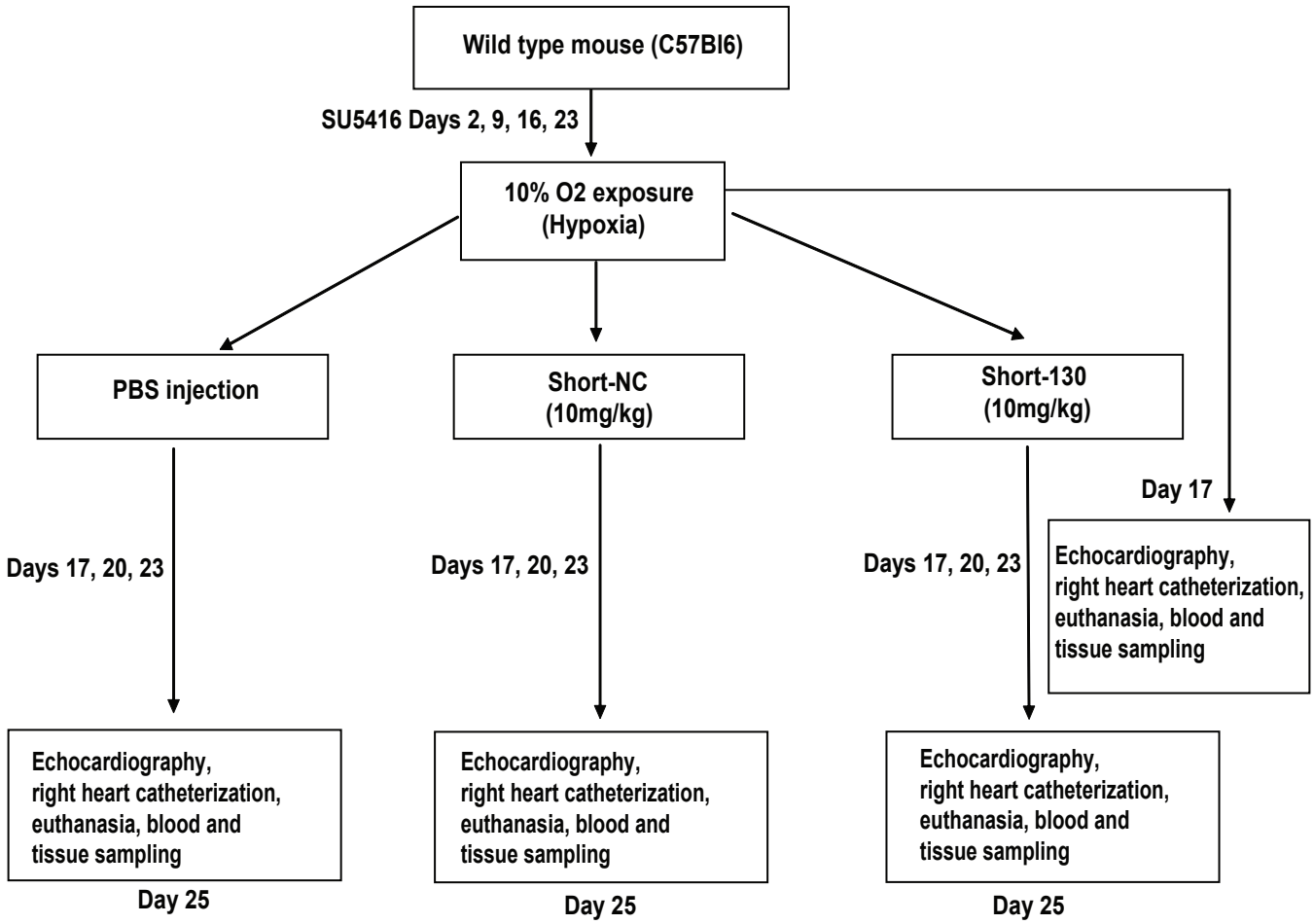

Bertero et al FigS23

A

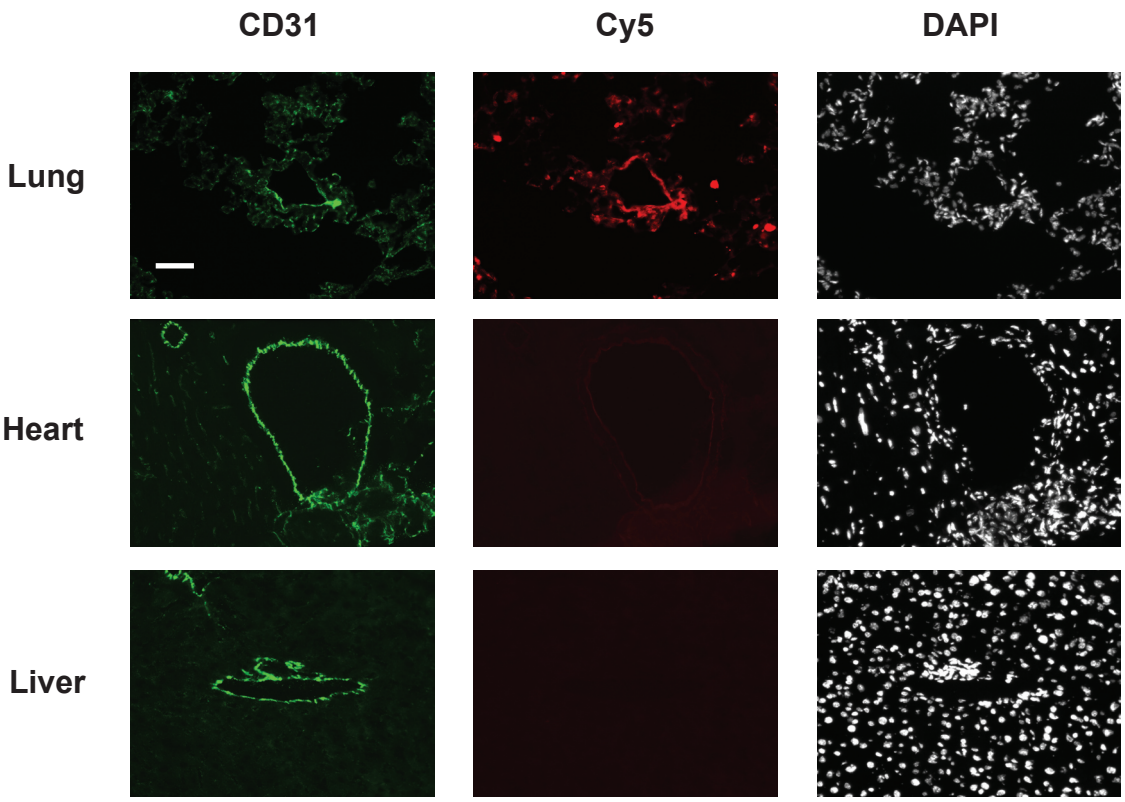

Mouse lung (post-Cy5-conjugated shortmer delivery)

B

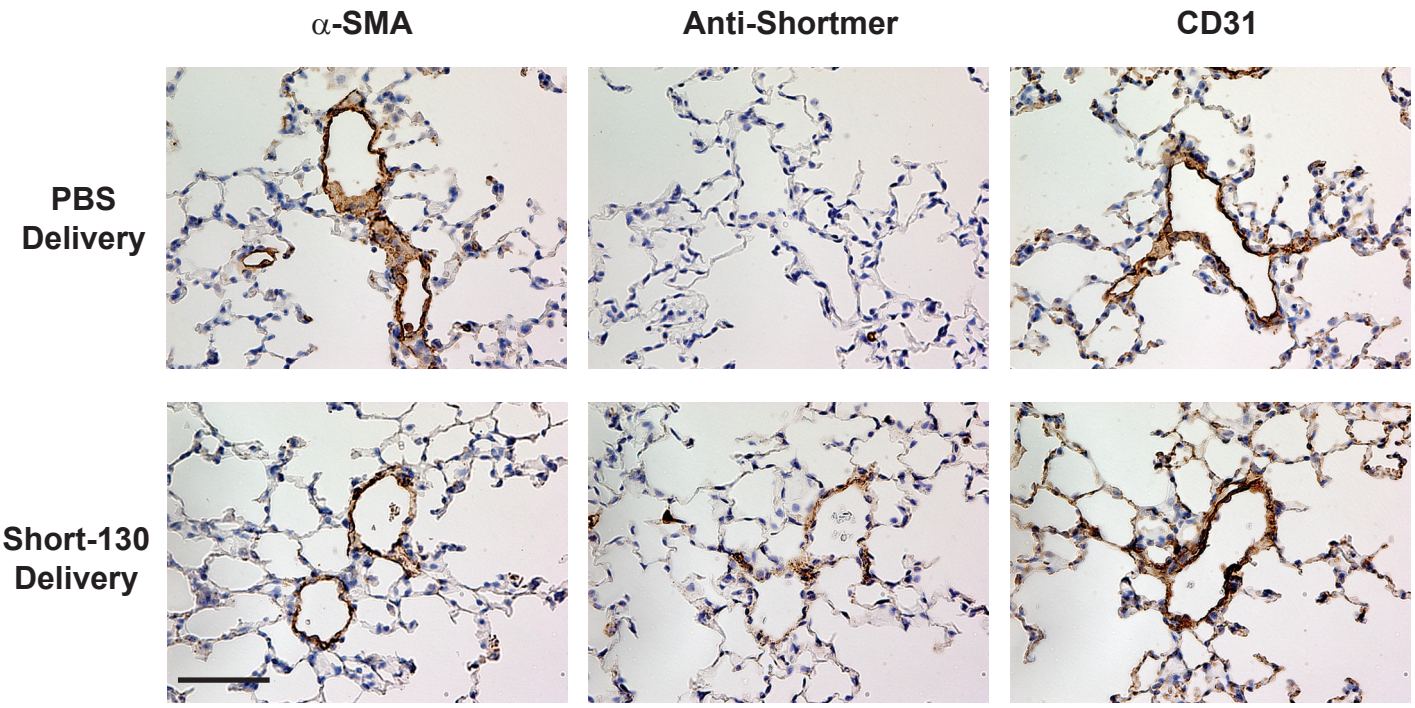

Mouse Lung (post-shortmer delivery)

Bertero et al FigS24

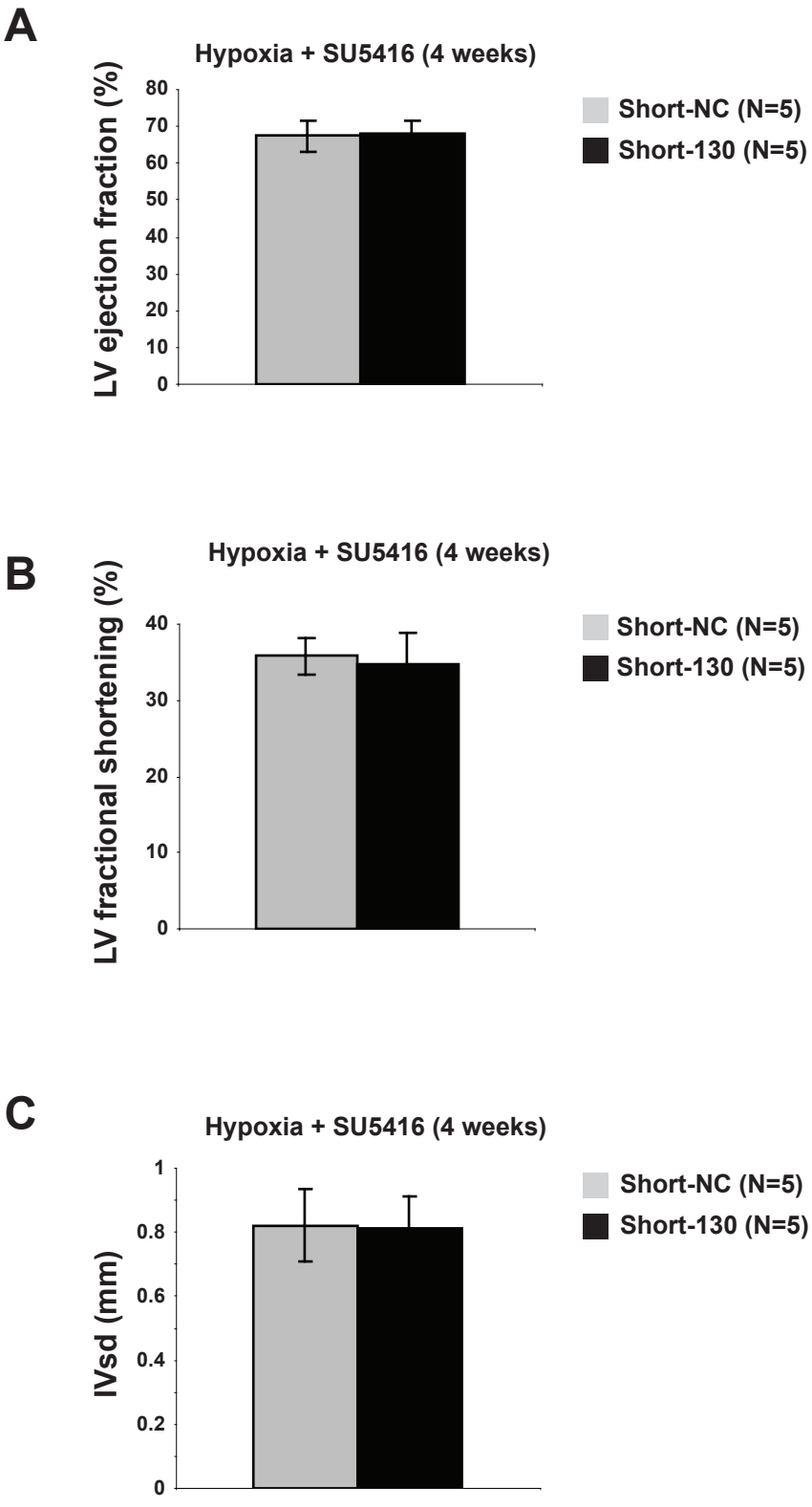

Bertero et al FigS25

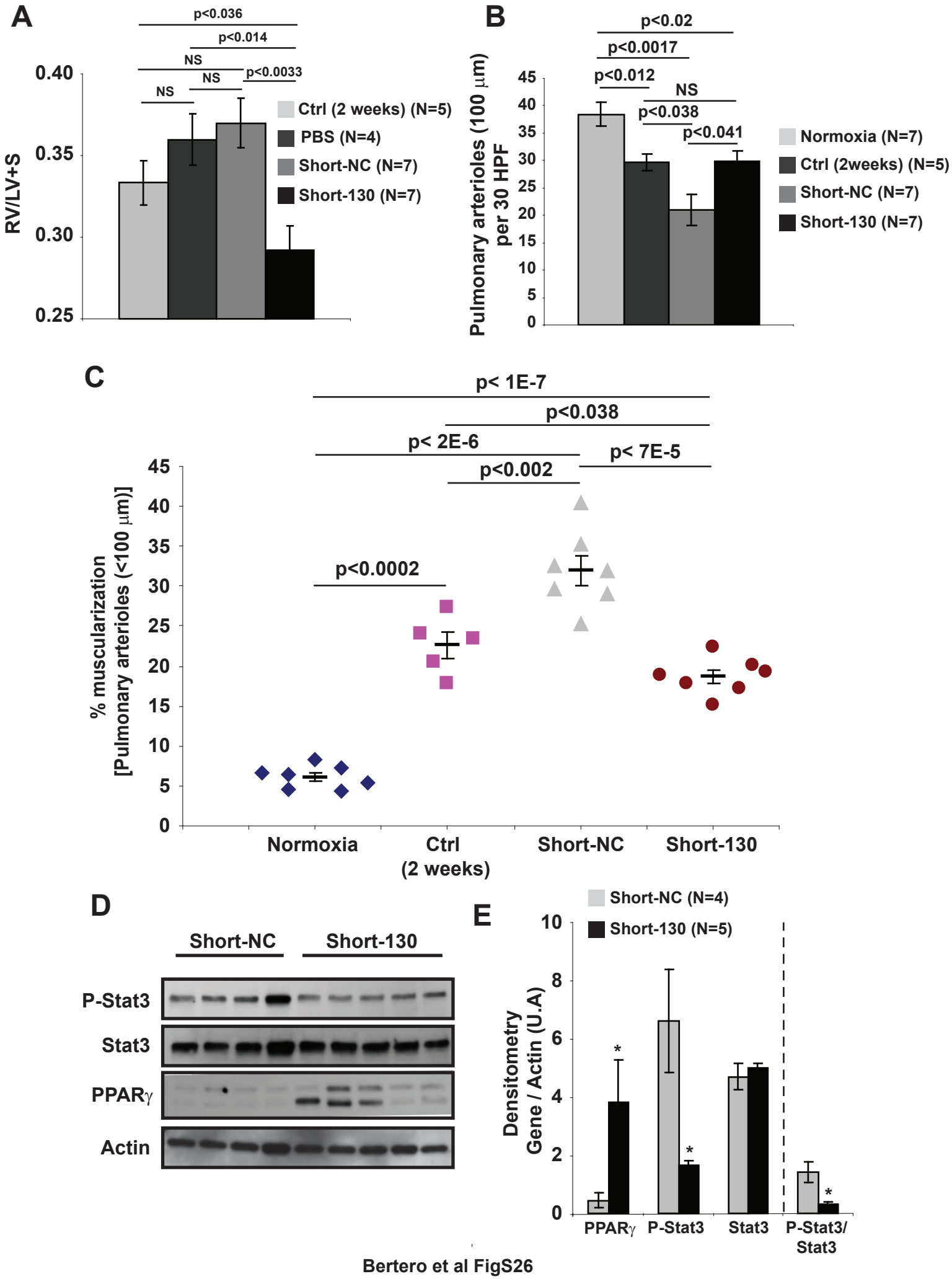

Bertero et al FigS26